

Impact of nuclear matter properties on the nucleosynthesis and the kilonova from binary neutron star merger ejecta

Giacomo Ricigliano^{1*}, Maximilian Jacobi² and Almudena Arcones^{1,3,4}

¹*Institut für Kernphysik, Technische Universität Darmstadt, Schlossgartenstr. 2, Darmstadt 64289, Germany*

²*Theoretisch-Physikalisches Institut, Friedrich-Schiller Universität Jena, Jena 07743, Germany*

³*GSI Helmholtzzentrum für Schwerionenforschung GmbH, Planckstr. 1, Darmstadt 64291, Germany*

⁴*Max-Planck-Institut für Kernphysik, Saupfercheckweg 1, Heidelberg 69117, Germany*

Accepted XXX. Received YYY; in original form ZZZ

ABSTRACT

Material expelled from binary neutron star (BNS) mergers can harbor r-process nucleosynthesis and power a Kilonova (KN), both intimately related to the astrophysical conditions of the ejection. In turn such conditions indirectly depend on the equation of state (EOS) describing matter inside the neutron star. Therefore, in principle the above observables can hold valuable information on nuclear matter, as the merger gravitational wave signal already does. In this work, we consider the outcome of a set of BNS merger simulations employing different finite-temperature nuclear EOSs. The latter are obtained from a Skyrme-type interaction model where nuclear properties, such as the incompressibility and the nucleon effective mass at saturation density, are systematically varied. We post-process the ejecta using a reaction network coupled with a semi-analytic KN model, to assess the sensitivity on the input EOS of the final yields and the KN light curves. Both of them are found to be non-trivially influenced by the EOS, with the overall outcome being dominated by the heterogeneous outflows from the remnant disk, hosting a variable degree of neutron-rich material. The dynamical ejecta can be more directly related to the EOS parameters considered, however, we find its role in the yields production and the KN emission too entangled with the other ejecta components, in order to infer solid correlations. This result highlights the strong degeneracy that intervenes between the merger outcome and the behaviour of the intrinsic nuclear matter, and places itself as a limit to the employment of EOS-constraining approaches of such kind.

Key words: stars: neutron – equation of state – nuclear reactions, nucleosynthesis, abundances – transients: neutron star mergers

1 INTRODUCTION

The recently born multi-messenger era, initiated by the first joint gravitational wave (GW) and electromagnetic (EM) detection of a binary neutron star (BNS) merger (Abbott et al. 2017a,b, 2019), has opened an independent astronomical window on the study of nuclear matter, in addition to direct neutron star (NS) measurements such as the mass-radius observations from NICER (Miller et al. 2019; Riley et al. 2019; Miller et al. 2021; Riley et al. 2021; Ludlam et al. 2022; Salmi et al. 2022). Many of the observable features of BNS mergers are strongly connected to the equation of state (EOS) of matter at the high densities found inside the NS, where typical values exceed nuclear saturation density. The merger GW signal encapsulates information on the masses of the original NSs and their tidal deformability, which are intimately linked to the EOS (see, e.g. Flanagan & Hinderer 2008; Hinderer et al. 2010; Hotokezaka et al. 2016; Abbott et al. 2017a; Annala et al. 2018; Tews et al. 2018; Abbott et al. 2018). Both the GW and EM emissions provide insight on the evolution of the merger remnant, which is strongly affected by the internal structure of the NS (see, e.g., Bauswein et al. 2012; Ravi & Lasky 2014; Bernuzzi et al. 2015; Radice et al. 2017; Margalit & Metzger 2017; Shibata et al. 2017; Bauswein et al.

2017; Rezzolla et al. 2018; Radice et al. 2018b). Furthermore, among the EM transients, the Kilonova (KN) reflects the properties of the radioactive material expelled in the process (Li & Paczynski 1998; Metzger et al. 2010), which depend on the thermodynamic evolution of the nuclear matter powering the emission. These dependencies also propagate to the study of the chemical evolution of the galaxy, to which the final yields of merger events are a relevant input (see, e.g., Thielemann et al. 2017; Côté et al. 2019).

The quantitative study of BNS mergers requires general-relativistic 3-dimensional hydrodynamical simulations, where a model for the high density EOS is necessary to describe the fluid pressure. The latter can have a major role in determining for example if and when the central remnant will collapse into a black hole (BH), how massive and extended the accretion torus will be, and the amount and composition of material expelled during different phases of the system’s evolution (Sekiguchi et al. 2016; Bovard et al. 2017; Radice et al. 2018c,a; Nedora et al. 2021b, 2022; Camilletti et al. 2022). These outcome details are then of fundamental importance for the nucleosynthesis harbored in the merger ejecta as well as for the subsequent KN emission. On one hand, the nuclear burning depends on the thermodynamics of the outflow, whereas for example a cold environment rich enough in neutrons such as the tidal ejecta sets the stage for a strong r-process to occur (Lattimer & Schramm 1974; Eichler et al. 1989; Freiburghaus et al. 1999; Rosswog et al. 2018;

* Contact e-mail: giacomo.ricigliano@gmail.com

Cowan et al. 2021, for a recent review on r-process). The yields of such event, which are typically calculated using a nuclear reaction network involving thousands of nuclear species (see, e.g., Winteler et al. 2012; Lippuner & Roberts 2017; Reichert et al. 2023), are thus affected by which outflow component dominates the merger ejection. On the other hand, the KN powered by the radioactive decay of the r-process elements, broadly depends on the overall mass of the ejecta, their opacity to optical photons, which is a function of the composition, their expansion velocity, and their spatial distribution (see, e.g., Arnett 1982; Pinto & Eastman 2000; Barnes & Kasen 2013; Tanaka & Hotokezaka 2013; Metzger & Fernández 2014; Perego et al. 2014b; Martin et al. 2015; Perego et al. 2017; Rosswog et al. 2018; Wollaeger et al. 2018; Kasen & Barnes 2019; Metzger 2020, for a recent review). The physics behind these dependencies is captured to different degrees of accuracy by a variety of KN models. Already only the first days of KN emission (when the ejecta is optically thick and it can be assumed to be in a local thermodynamic equilibrium (LTE) condition) can be synthetically reproduced through detailed radiative transfer simulations (see, e.g., Tanaka & Hotokezaka 2013; Kasen et al. 2017; Wollaeger et al. 2018; Bulla 2019, 2023; Shingles et al. 2023), radiation hydrodynamics simulations (Morozova et al. 2015; Wu et al. 2022; Magistrelli et al. 2024), or more approximated speed-oriented models (see, e.g., Grossman et al. 2014; Martin et al. 2015; Hotokezaka & Nakar 2020; Ricigliano et al. 2024).

Several works have explored the impact of the nuclear EOS model in BNS merger simulations, in some cases extending the analysis also to the composition of the ejected material and to the KN emission. The finite-temperature, composition-dependent EOSs considered were typically obtained from a pool of different nuclear models, derived from relativistic mean field and Skyrme density functional models (see, e.g., Lattimer & Swesty 1991; Steiner et al. 2013; Schneider et al. 2017; Bombaci & Logoteta 2018). These studies, therefore, varied many different EOS properties at the same time, and thus mostly assessed the impact of the degree of stiffness of the EOS, typically found to be degenerate with other characterizing merger parameters, such as the original binary mass ratio (see, e.g., Neilsen et al. 2014; Sekiguchi et al. 2016; Bovard et al. 2017; Radice et al. 2018b; Coughlin et al. 2018; Radice et al. 2018c; Most et al. 2019; Perego et al. 2019; Dietrich et al. 2020; Hammond et al. 2021; Nedora et al. 2021a; Perego et al. 2022a; Camilletti et al. 2022). More systematic investigations of specific EOS properties were carried out with different levels of sophistication in, e.g., Bauswein et al. (2010); Raithel et al. (2019); Fields et al. (2023); Blacker et al. (2024), which focused on thermal effects, or Most & Raithel (2021), focusing on the nuclear symmetry energy.

This work is intended as a reprise of the study conducted by Jacobi et al. (2023), where selected nuclear matter properties characterizing the nuclear EOS were varied systematically, and their impact on the merger dynamics, mass ejection, and GW emission was investigated. The study focused on the variation of the incompressibility and of the effective nucleon mass, which can affect the merger evolution on different levels, since both the cold and the thermal part of the EOS are modified. Here, we extend the analysis further, focusing on the nucleosynthesis harbored in the merger ejecta, and predicting synthetic light curves of the subsequent KN transient. The paper is organized as follows. We describe the initial setup and the framework used to post-process data from the merger simulations in Sec. 2. In Sec. 2.1, we list the EOS models considered. We then describe the procedure for the extraction of fluid elements in Sec. 2.2, the setup for the nucleosynthesis calculations in Sec. 2.3, and the KN semi-analytic model in Sec. 2.4. We dedicate Sec. 3 to the analysis of the general properties of the ejecta (Sec. 3.1), their final composition

(Sec. 3.2), and the corresponding KN light curves (Sec. 3.3). The discussion on the reliability of our results is then extended in Sec. 3.4. Finally, the main findings are reported, together with some final remarks, in Sec. 4.

2 METHODS

This work is based on a series of 3D general-relativistic hydrodynamical simulations published in Jacobi et al. (2023). All the simulations follow the merger of a symmetric binary neutron star system with masses $1.365 M_{\odot}$. A different nuclear EOS was used for each simulation (see Sec. 2.1). The simulations were performed using the WhiskyTHC code (Radice & Rezzolla 2012) within the EinsteinToolkit suite (Haas et al. 2020). Neutrino emission and absorption were modeled by a grey leakage scheme and a one-moment neutrino transport scheme, respectively (Radice et al. 2018c). For further details on the simulations setup, we refer the reader to Jacobi et al. (2023).

2.1 EOS models

We consider seven EOSs calculated using the SROEOS code (Schneider et al. 2017). The latter provides EOSs based on a Skyrme functional, tabulated as a function of density, temperature, and electron-fraction. Of the seven EOSs, five were first used in Yasin et al. (2020) and two were newly created in Jacobi et al. (2023). In the EOSs computation, the nuclear matter properties at saturation density were systematically varied, specifically the incompressibility K , the effective nucleon mass m^* , the symmetry energy E_{sym} , the binding energy B , and the saturation density n_0 . Furthermore, the Shen EOS (Shen et al. 1998) is considered for the sake of comparison. In Table 1, we summarize the EOS models used in this work. We report the values of the nuclear matter properties, together with the tidal deformability and radius of the cold non-rotating neutron stars from the initial binary. We exclude the model LS175[†] from our analysis, since this leads to prompt collapse of the merger remnant and thus negligible amount of ejecta.

The fiducial model LS220[†] is based on the L&S EOS with an incompressibility value of 220 MeV (Lattimer & Swesty 1991). First, the incompressibility is varied within uncertainties predicted by chiral effective field theory calculations (Hebeler et al. 2011; Drischler et al. 2016, 2019), leading to the models LS175[†] and LS255[†]. Subsequently, the effective mass is changed from the LS220[†] value of $m^* = m_n$, where m_n is the nucleon mass, to $m^* = 0.8 m_n$ ($m_{0.8}^*$) and $m^* = 0.634 m_n$ (m_{S}^*), which is the value found in the Shen EOS. The remaining nuclear matter properties are then modified to match the corresponding values of the Shen EOS, starting from the model m_{S}^* . The matched parameters include first K , and then E_{sym} , n_0 and B , leading to the models $(m^*K)_{\text{S}}$ and SkShen respectively (see Yasin et al. 2020; Jacobi et al. 2023, for a more detailed overview of the EOS models).

As found by Jacobi et al. (2023), the incompressibility affects the slope of the cold pressure around saturation density, with higher K values leading to steeper pressure-density profiles. The effective nucleon mass instead impacts both the cold and the thermal contributions to the pressure. Within this framework, a lower effective mass leads to a larger slope parameter L and therefore an increase of the EOS' stiffness at lower densities. Furthermore, lower m^* values, increase the thermal contribution to the pressure.

Table 1. List of employed EOS models and their nuclear matter properties at saturation density. The value of the effective nucleon mass is given in terms of the nucleon mass $m_n = 939.5654$ MeV. We also report the corresponding values of the reduced tidal deformability $\tilde{\Lambda}$ and NS radii of initial binaries. The model LS175[†] is highlighted in grey since it is excluded from our analysis due to the prompt collapse of the merger remnant. Red and blue values indicate the models used to analyse the systematic variation of the effective nucleon mass and the incompressibility, respectively.

EOS model	m^* [m_n]	B [MeV]	K [MeV]	E_{sym} [MeV]	L [MeV]	ρ_0 [10^{14} g cm ⁻³]	$\tilde{\Lambda}$	R_{NS} [km]
LS175 [†]	1.0	16.0	175	29.3	73.7	2.57	358.9	12.1
LS220 [†]	1.0	16.0	220	29.3	73.7	2.57	606.2	12.7
LS255 [†]	1.0	16.0	255	29.3	73.7	2.57	661.1	13.0
$m_{0.8}^*$	0.8	16.0	220	29.3	79.3	2.57	698.4	12.9
m_S^*	0.634	16.0	220	29.3	86.5	2.57	765.4	13.2
$(m^*K)_S$	0.634	16.0	281	29.3	86.5	2.57	975.0	13.5
SkShen	0.634	16.3	281	36.9	109.4	2.41	1295.5	14.5
Shen	0.634	16.3	281	36.9	110.8	2.41	1220.8	14.5

2.2 Ejecta extraction

In order to perform the nucleosynthesis calculations, we follow the ejected matter using Lagrangian tracer particles. We obtain their trajectories by integrating the fluid velocity fields backwards in time until they reach a temperature above 10 GK. The integration is performed in a post-processing step based on the simulation output. For an overview of the advantages and disadvantages of backward tracer particle evolution see, e.g., Sieverding et al. (2023), while for an assessment on the impact of the neglected dynamics-nucleosynthesis coupling, see Magistrelli et al. (2024).

The tracer particles are separated into two sets. *Set 1* is initialized on a spherical surface with a radius of $R \approx 1500$ km, in regular time intervals of $\Delta t \approx 1$ ms, in order to record matter that exits the domain boundaries within the simulated time. A similar scheme was used in Fujibayashi et al. (2020) but for 2D simulations. *Set 2* is initialized inside the spherical volume at the end of the simulation, to account for ejected matter that did not reach the outer boundary by the end of the simulation. Tracer particles are only created where the matter fulfills the Bernoulli criterion, i.e. in the fluid element satisfying the condition $-hu_t > h_\infty$, where $h = 1 + \epsilon + P/\rho$ is the relativistic specific enthalpy, u_t is the time component of its four-velocity and $h_\infty = \lim_{\rho, T \rightarrow 0} h$ is the asymptotic specific enthalpy (see, e.g., Foucart et al. 2021, for an overview of ejection criteria).

The initial distribution of tracer particles is critical to ensure that the fluid motion is sufficiently well resolved at all times relevant for the nucleosynthesis (see, e.g., Bovard & Rezzolla 2017, for an overview of different tracer particle distribution schemes). In the following, we outline the method that we use to set the starting points for the backward evolution of our tracer particles.

For *set 1*, we divide the spherical surface into a rectangular grid where each cell has the same solid angle. Similarly, we divide the sphere of *set 2* into cubic cells of equal volume. Next, we calculate the mass contained in each cell. For *set 1*, the masses are calculated by integrating the radial rest-mass flux over the cell area:

$$m_1 = R^2 \Delta t \int_{\text{cell}} \rho V^r d\Omega, \quad (1)$$

where the radial fluid velocity is given by $V^r = \alpha v^r - \beta^r$, with α the lapse function, v^r the radial 3-velocity and β^r the radial shift-vector. We split each cell with a mass greater than a maximum mass $m_{\text{max}} \approx 10^{-6} M_\odot$ into 4 smaller cells with equal solid angles. This procedure is repeated for all timesteps until all cells contain less mass than m_{max} . The masses for *set 2* are instead given by the volume integral of the rest-mass density over the cell volume:

$$m_2 = \int_{\text{cell}} \rho dV. \quad (2)$$

Equivalently to *set 1*, we split all cells with $m_2 > m_{\text{max}}$ into 8 smaller cells with equal volume until all cells have a mass below m_{max} . Finally, a tracer particle is placed at a random location in each cell in order to cancel the bias introduced by the original regular grid. This procedure ensures that the mass of all tracer particles is small ($< 10^{-6} M_\odot$), while at the same time the regions of very low rest-mass density are not underresolved, since the minimum spatial resolution is given by the initial grid.

In Jacobi et al. (2023), the ejected matter is classified on the basis of its properties at an extraction radius of 300 km. The dynamical ejecta are defined as the material fulfilling the geodesic criterion $-u_t > 1$, as in Nedora et al. (2021b); Combi & Siegel (2023). Such ejecta are further divided depending on their electron fraction, whereas fluid elements with $Y_e \leq 0.1$ are classified as tidal ejecta and fluid elements with $Y_e > 0.1$ as shock-heated ejecta. Finally, matter that fulfills the Bernoulli but not the geodesic criterion is categorized as disk ejecta. We find that the resulting distinction generally agrees with those obtained by employing different criteria, such as separating the ejecta according to a defined ejection time or on the basis of the remnant density evolution. Therefore, here we adopt the same classification scheme in order to be consistent across the two studies.

Note that in the previous analysis from Jacobi et al. (2023), the extraction radius is used to identify the matter ejected, while here the ejection criterion is evaluated at the latest possible time for each fluid element. Therefore, the total ejecta mass reported in this work is slightly different and should be more exact.

2.3 Nucleosynthesis calculations and heating treatment

For each merger model, we post-process the thermodynamic evolution of the ejecta using the nuclear reaction network WinNet (Reichert et al. 2023) in order to determine their nucleosynthesis history. In particular, we perform network calculations on ~ 15000 tracers per merger simulation, and we investigate the effects of reducing this number on the final yields by specifically selecting a subset which is representative of the ejecta composition. We discuss the details of this tracer selection in Appendix A, where we note that a fraction of less than 10% of the total tracers is enough to reproduce the same results without a significant loss in accuracy.

The nuclear reaction network consists of 6545 nuclear species linked with a set of temperature-dependent reaction rates imported from the JINA REACLIB library (Cyburt et al. 2010). The latter includes available experimental rates, together with theoretical rates largely based on the FRDM nuclear mass model (Möller et al. 2016). Spontaneous, neutron-induced and β -delayed fissions are treated as presented in Panov et al. (2001), while neutrino-induced reactions

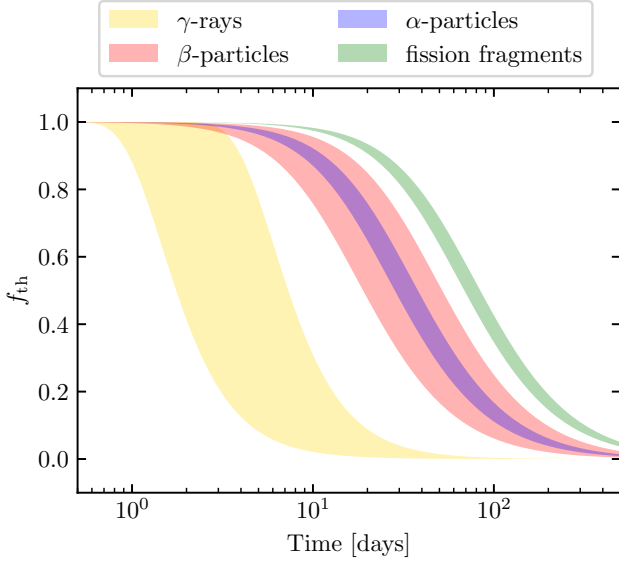


Figure 1. Thermalization efficiency of γ -rays, electrons, α -particles and fission fragments as a function of time post-merger for typical particle injection energies, computed using Eq. (3) and Eq. (4). The inefficiency timescale is computed by assuming a spherical outflow with uniform density, total mass $M_{\text{ej}} = 0.01 M_{\odot}$ and characteristic velocity $v_{\text{ej}} = 0.1 c$. We consider the following ranges for the particle initial energies: $E_{0,\gamma} = 0.2 - 1.5$ MeV, $E_{0,\beta} = 0.2 - 1.5$ MeV, $E_{0,\alpha} = 5 - 9$ MeV and $E_{0,\text{ff}} = 100 - 150$ MeV (Barnes et al. 2016).

are not included since they are expected to play a subdominant role at the characteristic densities and temperatures of the fluid trajectories. Each nucleosynthesis calculation starts when the fluid temperature decreases to 7 GK, with the initial composition being determined assuming nuclear statistical equilibrium (NSE). The tracer trajectory is then extrapolated past the simulation time by assuming adiabatic, homologous expansion. We record until 1 Gyr the elemental abundances evolution and the radioactive energy output, which we separate into the main contributions from β -decays, α -decays, and fissions.

In order to estimate the associated KN emission, we treat the energy release by distinguishing between different energy carriers, i.e. β -particles, α -particles, γ -rays, and fission fragments. We import from the Evaluated Nuclear Data File (ENDF/B-VIII.0, International Atomic Energy Agency) the measured average energies of β - and α -decay products for each parent nuclide. If data is not available we adopt the Q-value fractions suggested by Barnes et al. (2016), i.e. we assume that typically in β -decays $\sim 20\%$ of the energy is carried by electrons, $\sim 45\%$ by γ -rays and the remaining $\sim 35\%$ escapes in the form of neutrinos, while in α -decays roughly the entirety of the energy budget is retained by α -particles. Furthermore, we assign all the energy produced in fission processes to the kinetic energy of the fission products.

Each channel deposits energy differently within the ejecta, with an efficiency $f_{\text{th},i}(t) = \frac{\dot{Q}_{\text{dep},i}(t)}{\dot{Q}_{\text{r},i}(t)}$ gradually decreasing in time, where $\dot{Q}_{\text{r},i}(t)$ and $\dot{Q}_{\text{dep},i}(t)$ are the radioactive heating rate and the energy deposition rate for the channel i , respectively. Following Barnes et al. (2016), for an outflow represented by a sphere with uniform density,

the thermalization efficiency can be approximately described by

$$f_{\text{th},p}(t) = \frac{\ln \left[1 + 2 \left(\frac{t}{t_{\text{ineff},p}} \right)^2 \right]}{2 \left(\frac{t}{t_{\text{ineff},p}} \right)^2}, \quad (3)$$

$$f_{\text{th},\gamma}(t) = 1 - \exp \left[- \left(\frac{t}{t_{\text{ineff},\gamma}} \right)^{-2} \right], \quad (4)$$

with Eq. (3) and Eq. (4) valid for massive particles and γ -rays respectively. Here t_{ineff} is the characteristic time at which thermalization becomes inefficient, i.e. when the expansion timescale becomes shorter than the thermalization timescale. The latter is in general dependent on the type of decay product, on its initial energy E_0 , and on the material density. Within the uniform density approximation, for ejecta with mass M_{ej} and characteristic velocity v_{ej} , the inefficiency time in the case of massive particles follows $t_{\text{ineff}} \propto E_{0,p}^{-1/2} M_{\text{ej}}^{1/2} v_{\text{ej}}^{-3/2}$.

In the case of γ -rays instead, $t_{\text{ineff}} \propto M_{\text{ej}}^{1/2} v_{\text{ej}}^{-1}$, with a variation of a factor of a few depending on whether the dominant interaction is Compton scattering ($E_{0,\gamma} \gtrsim 1$ MeV) or photoionization ($E_{0,\gamma} \lesssim 1$ MeV) (Barnes et al. 2016). As shown in Fig. 1, for typical fluid conditions and initial energy of decay products, the thermalization of γ -rays becomes inefficient already after ~ 1 day, while massive particles are able to efficiently deposit their energy into the medium for several days, with the more massive and slower fission fragments having the largest efficiency at each time.

2.4 Kilonova model

We couple the nucleosynthesis calculations to a semi-analytic KN model in order to obtain synthetic KN light curves. We construct an anisotropic KN scheme informed by the ejecta geometry, and we model an approximate energy transfer in order to account for the diffusion and the emission of photons. In particular, we start from the model for spherically symmetric ejecta presented by Hotokezaka & Nakar (2020) and based on the supernova model from Arnett (1982). While the latter describes the ejecta using a single zone approximation, the model from Hotokezaka & Nakar (2020) accounts for the ejecta stratification by computing the contribution to the luminosity coming from each spherical shell with mass m_i , velocity v_i , and opacity κ_i . The ejecta density is assumed to follow the radial profile

$$\rho(t, v) = \rho_0(t) \left(\frac{v}{v_0} \right)^{-4.5}, \quad (5)$$

with v ranging between the minimum ejecta velocity v_0 and the maximum velocity v_{max} , and ρ_0 being defined by fixing the total ejecta mass M_{ej} . The model is based on the first law of thermodynamics for a radiation dominated gas, i.e.

$$\frac{dE_i}{dt} = -\frac{E_i}{t} + m_i \dot{\epsilon}(t) - L_i(t), \quad (6)$$

where E_i is the i -th shell internal energy, $\dot{\epsilon}$ is the specific radioactive heating rate and L_i is the shell contribution to the luminosity. The total bolometric luminosity is approximated by

$$L(t) = \sum_i \text{erfc} \left(\sqrt{\frac{t_{\text{diff},i}}{2t}} \right) \frac{E_i}{\min(t_{\text{diff},i}, t) + \frac{v_i t}{c}}, \quad (7)$$

with $t_{\text{diff},i} = \tau_{\gamma,i} v_i t c^{-1}$ the photon diffusion timescale and $\tau_{\gamma,i}$ the photon optical depth, defined as

$$\tau_{\gamma,i}(t) = \int_{v_i}^{v_{\text{max}}} \kappa(v) \rho(v) t dv. \quad (8)$$

We characterize the ejecta opacity radial profile $\kappa(v)$ by employing a step function with an average inner opacity value κ_{in} , an average outer value κ_{out} in general different from the first, and the step v_{step} located at the approximate interface between the dynamical ejecta and the disk ejecta. The complementary error function term in Eq. (7) approximately describes the fraction of energy that escapes from each shell. For a diffusion timescale which is greater than the expansion timescale, photons are essentially trapped in the medium and most of the radiation energy does not contribute to the instantaneous luminosity. On the other hand, when the diffusion timescale is shorter than the expansion timescale, radiation escapes almost freely and the contributing fraction is ~ 1 .

Following Martin et al. (2015); Perego et al. (2017); Barbieri et al. (2019, 2020); Camilletti et al. (2022); Ricigliano et al. (2024), we generalize the spherical model to the anisotropic case by assuming axisymmetry with respect to the system rotational axis and by discretizing the ejecta along the polar angle θ direction in 15 slices uniform in θ . To each angular bin we assign the total mass of the fluid elements ejected at the corresponding latitude. The ejection angle is evaluated using the element last tracked displacement, i.e. we assume to follow the ejecta long enough to resolve their asymptotic direction. Concurrently, we also associate to the angular bin a mass-weighted average velocity together with a minimum and a maximum velocity value which are represented by the 1% and the 99% mass-weighted percentiles of the bin tracers velocity distribution respectively, in order to exclude irrelevant outliers. The velocity of each tracer is evaluated using the asymptotic definition $v_{\infty} = \sqrt{1 - \left(\frac{h_{\infty}}{hu_t}\right)^2}$, following, e.g., Fujibayashi et al. (2020). Finally, we compute mass-weighted average opacities for the inner and the outer part of the angular bin, on the basis of the initial electron fraction Y_e . The opacity parametrization is imported from Tanaka et al. (2020), which perform systematic atomic structure calculations for all the elements between $26 < Z < 88$, and compute a representative Planck grey opacity for each composition in a set characterized by the value of initial Y_e . Although approximate, these estimates return a reasonable representation of the overall opacity in the ejecta with typical densities $\rho \sim 10^{-13} \text{ g cm}^{-3}$ and temperatures $T \lesssim 20000 \text{ K}$, where thermal photons diffusion is dominated by bound-bound transitions in mildly-ionized r-process elements.

The latitudinal bin mass is isotropized with a factor $4\pi/\Omega$, where Ω is the bin angular size, and it is injected together with the bin characteristic velocities, opacities and the thermalized heating rate from the nucleosynthesis calculations in the spherical KN model, in order to compute the bin isotropized contribution to the total bolometric luminosity. The latter is then obtained by summing all the angular contributions rescaled back to the original bin size.

We describe the radiation escaping from the outflow as an approximate black-body with a surface represented by the ejecta photosphere. At each latitude, the photosphere position r_{ph} in time is tracked by imposing the condition $\tau_{\gamma}(r_{\text{ph}}) \sim 1$ to the photon optical depth, and the photospheric effective temperature T_{ph} is computed using the Stefan-Boltzmann law. In a luminosity peak timescale, the photosphere recedes inwards in the outflow, and its effective temperature decreases from $\sim 10000 \text{ K}$ to a few 1000 K . We impose a minimum to T_{ph} as the photosphere starts to follow the electron-ion recombination in the late expanding ejecta (Barnes & Kasen 2013), and we parametrize this temperature floor with the local composition. We choose as representative bracketing values $T_{\text{floor}}^{\text{La}} = 2000 \text{ K}$ for Lanthanides-polluted compositions with a low initial electron fraction $Y_e \lesssim 0.2$ and $T_{\text{floor}}^{\text{Ni}} = 4000 \text{ K}$ for Lanthanides-poor compositions with $Y_e \gtrsim 0.3$.

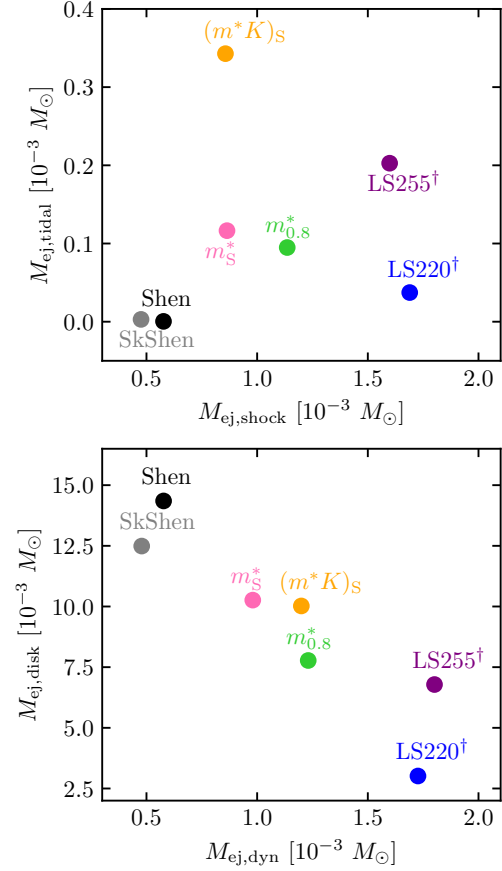


Figure 2. Total masses of each ejecta component for the different EOS models: tidal ejecta versus shock-heated ejecta (top panel) and dynamical ejecta versus disk ejecta (bottom panel). The masses are extracted at the end of the simulations and are classified according to the procedure described in Sec. 2.2.

We derive the AB magnitudes at a given frequency ν as

$$m_{\text{AB},\nu}(t) = -2.5 \log_{10}(f_{\nu}(t)) - 48.6, \quad (9)$$

where $f_{\nu}(t)$ is the observed flux, i.e.

$$f_{\nu}(t) = \frac{1}{4\pi D_L^2} \int p(\theta, \theta_{\text{view}}) \frac{L_{\text{iso}}(\theta, t)}{\sigma_{\text{SB}} T_{\text{ph}}^4(\theta, t)} B_{\nu}(T_{\text{ph}}(\theta, t)) d\theta. \quad (10)$$

Here D_L is the luminosity distance from the source, which we fix to 40 Mpc , i.e. the value inferred for the gravitational wave signal GW170817, while $L_{\text{iso}}(\theta, t)$ is the isotropized bolometric luminosity contribution from the angular bin at θ , $B_{\nu}(T)$ is the Planck distribution, σ_{SB} is the Stefan-Boltzmann constant and $p(\theta, \theta_{\text{view}})$ is the flux projection factor in the direction of the observer at a viewing angle θ_{view} .

3 RESULTS

3.1 Ejecta properties

As investigated in many previous works (see, e.g., Bauswein et al. 2010; Hotokezaka et al. 2013; Sekiguchi et al. 2016; Radice et al. 2018c; Nedora et al. 2021a), the EOS strongly influence the evolution of the binary system in its merging and post-merging phase, impacting the amount of dynamical and disk ejecta. Figure 2 shows

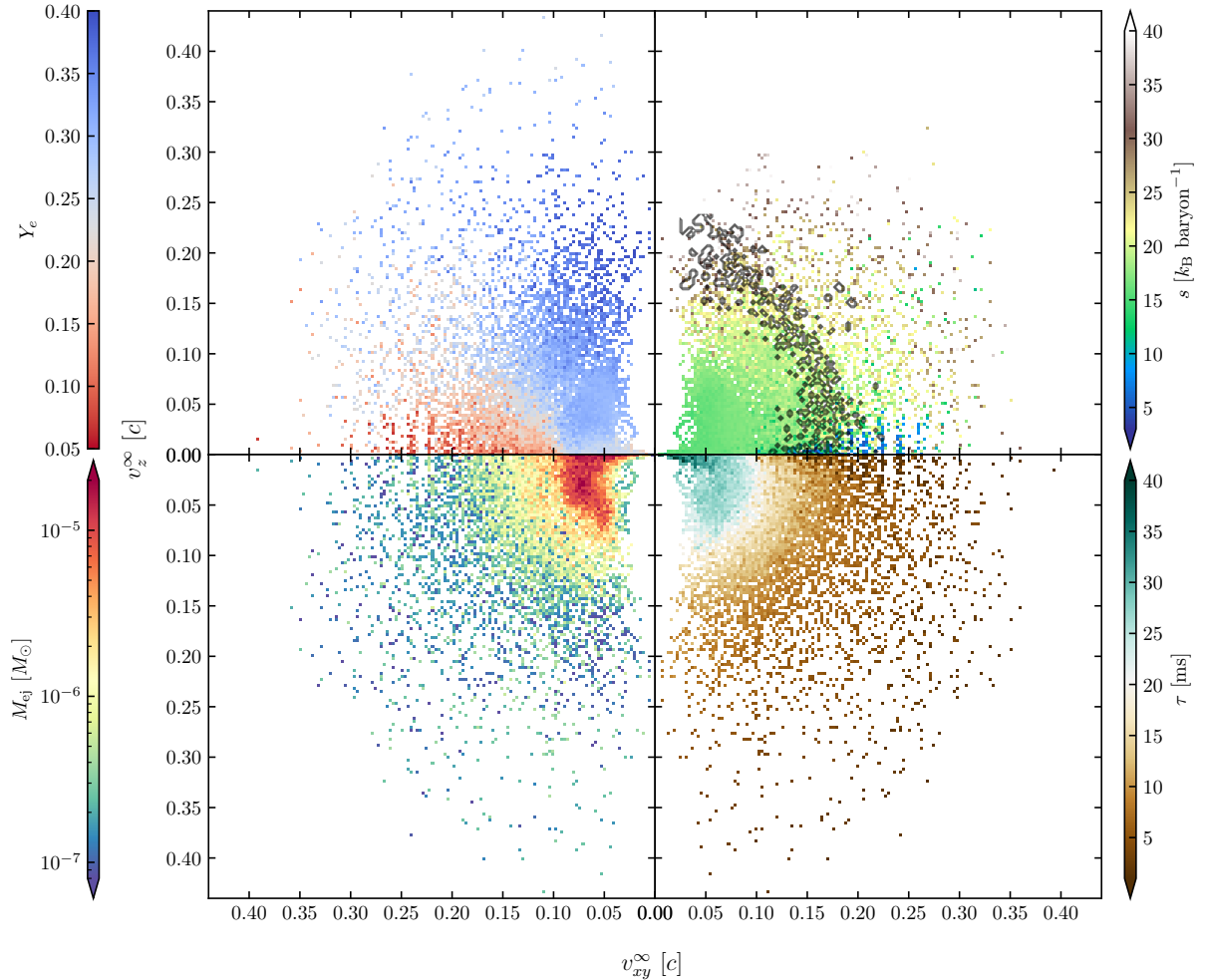


Figure 3. Representation of tracers on a velocity space grid for the model m_S^* . Points in the grid are colour-coded relating to the mass-weighted average electron fraction (top left panel), specific entropy (top right panel) and expansion timescale (bottom right panel), evaluated at a tracer temperature of ~ 5.8 GK. The bottom left panel shows the tracer’s mass distribution. The dark grey interface in the top right panel represents the approximative boundary between the slower disk ejecta and the faster dynamical ejecta, as computed using the geodesic criterion.

the masses of the ejecta components (as defined in Sec. 2.2) for all the models considered in this work. The dynamical ejecta are split into tidal and shock-heated ejecta (top panel of Fig. 2). Jacobi et al. (2023) found that the mass of the shock-heated component increases for higher pressures at saturation density, while the mass of the tidal component grows with the slope of the pressure as a function of density, in the same density regime. In particular, the models that differ only in the incompressibility (LS220[†] and LS255[†] as well as m_S^* and $(m^*K)_S$) exhibit roughly the same amount of shock-heated ejecta but vary considerably in the amount of tidal ejecta. On the other hand, in the models that differ only in the effective mass (LS220[†], $m_{0.8}^*$ and m_S^*), a smaller variation in the amount of tidal ejecta is found, while the amount of shock-heated ejecta varies considerably. The models SkShen and Shen do not exhibit any ejected material with $Y_e \leq 0.1$. In these models, the tidally ejected matter is reached by shocks from the merger interface very quickly, and all of its content is thus reprocessed towards higher electron fractions.

The amount of secular ejecta is highly dependent on the final fate of the central remnant (see, e.g., Fujibayashi et al. 2023). Mergers that result in a long-lived massive neutron star exhibit a larger accretion disk (since otherwise roughly half of the disk is accreted upon

collapse), leading to more ejecta from the accretion disk system. Furthermore, the ejection of the matter is enhanced by the reabsorption of neutrinos emitted by the remnant (Perego et al. 2014a; Just et al. 2015; Radice et al. 2018d) and spiral-wave winds driven by its oscillations (Nedora et al. 2019, 2021b).

In the model LS220[†], a hyper-massive neutron star forms after the merger and survives for ~ 8 ms. Consequently, in such a case the disk ejecta mass is very small. All other models considered in this work do not form a BH in the simulated time ($\sim 40 - 50$ ms). For them, the registered mass of the disk ejecta roughly increases with the stiffness of the underlying EOS, and it is significantly larger than that of the dynamical ejecta. However, we note that this trend is far from solid, since there is still matter ejected at the end of each simulation, and thus the mass values are only lower limits. In addition, it is expected that in all models a sizable fraction of the accretion disk will also be ejected on timescales of seconds due to alternative mechanisms, such as viscous heating (see, e.g., Hotokezaka et al. 2013; Fernández et al. 2019; Fujibayashi et al. 2020; Fahlman & Fernández 2022).

Despite the different masses of the ejecta components, many general features are consistent across all models. Figure 3 shows the distribution of the electron fraction Y_e , specific entropy s , mass M_{ej} ,

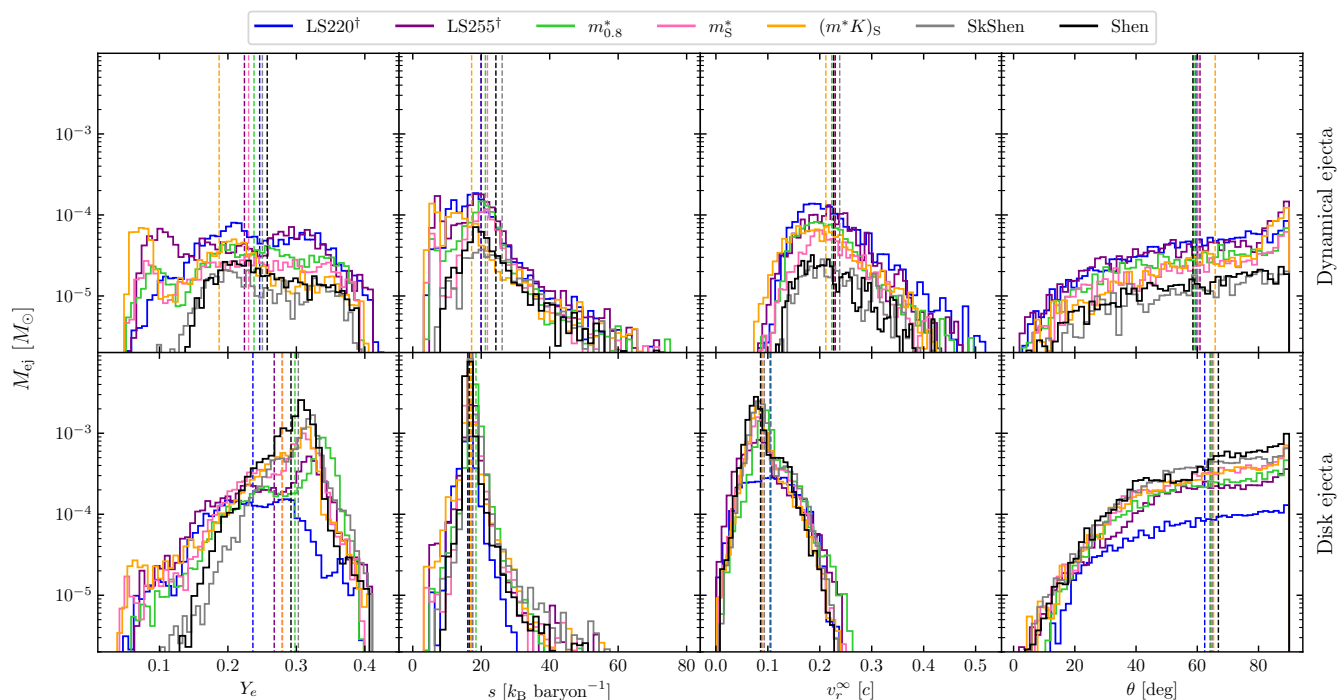


Figure 4. Ejecta mass histograms as a function of the electron fraction Y_e , the specific entropy s , the asymptotic radial velocity v_r^∞ and the polar angle of ejection θ , evaluated at a tracer temperature of ~ 5.8 GK, for the different EOS models, separately for the dynamical ejecta (top panels) and for the early disk ejecta (bottom panels). Vertical dashed lines represent the mass-weighted average values of each quantity.

and expansion timescale $\tau = r(v_r^\infty)^{-1}$ (all of which evaluated at $T \sim 5.8$ GK) versus their equatorial and polar asymptotic velocity for the model m_S^* . The dynamical ejection channel operates within the first ~ 10 ms post-merger, unbinding neutron-rich ($Y_e \lesssim 0.1$), low-entropy ($s \lesssim 10 k_B \text{ baryon}^{-1}$) material, predominantly along the equatorial plane, with velocities $\sim 0.15 - 0.35 c$. The shock-heated ejecta are launched more isotropically with higher entropies up to $\sim 40 k_B \text{ baryon}^{-1}$, traveling at velocities up to $\sim 0.45 c$. This material is heated significantly and thus positron captures increase the electron fraction to $0.1 \lesssim Y_e \lesssim 0.4$. The electron fraction gradually increases with the latitude, as a result of the lower density and higher entropy in the polar region. In addition, despite having velocities similar to those of the tidal component, the temperature of the shocked matter reaches 5.8 GK only at later times because it is initially hotter. Its expansion timescale is of the order of ~ 10 ms, compared to that of the tidal ejecta, which is $\lesssim 5$ ms.

Outflows from the disk emerge after ~ 10 ms post-merger, with lower velocities $\lesssim 0.15 c$ and correspondingly longer expansion timescales up to ~ 40 ms. This component shows fairly constant entropies $s \sim 20 k_B \text{ baryon}^{-1}$ and intermediate values of the electron fraction $0.15 \lesssim Y_e \lesssim 0.4$. The disk ejecta is launched in all directions, with its mass density decreasing towards higher latitudes. However, it does not fully cover the polar area ($\theta \lesssim 20^\circ$), because it is mainly driven by the remnant density waves traveling on the equatorial plane. In addition, neutrino absorption mostly impacts the outer exposed layers of the disk, causing the matter ejection to be more efficient at intermediate latitudes. The transition between dynamical ejecta and disk ejecta is depicted in Fig. 3 as a dark grey, slightly prolate, thick interface where material from different ejection mechanisms is present.

The mass-weighted histograms of the ejecta properties for the dif-

ferent models are shown in Fig. 4. The electron fraction and the entropy distributions of the dynamical ejecta have a systematic double-peak structure due to the tidal and the shock-heated component. The tidal component forms the low Y_e , low entropy peak, which is present in all models except for the SkShen and Shen EOSs, and it is enhanced in the models LS255[†] and $(m^*K)_S$ (see the discussion above). Instead, the shock-heated component is responsible for the higher Y_e plateau and the second peak at larger entropies.

Regarding the disk ejecta, the electron fraction distribution typically peaks at $Y_e \approx 0.3$. This peak is caused by the absorption of neutrinos in the ejecta above the disk (see Jacobi et al. (2023) for more information), and constitutes the largest fraction of the disk ejecta. The same matter also forms the peak in the velocity histogram at $v_r^\infty \approx 0.08 c$. Such component is missing in the LS220[†] model, since the collapse of the remnant into BH leads both to a suppression of the ejection and to a reduction in the neutrino reprocessing to which the already present ejecta is exposed. Notably, the specific position of the high Y_e peak, as well as the overall average Y_e in the ejecta, does not exhibit a clear correlation with the amount of matter expelled from the disk. It is instead clearer a dependency of the peak position on the disk latitudinal extension, which partially shields the ejecta from neutrino irradiation. Thus, for the model $m_{0.8}^*$, where the disk is considerably thinner than all the other non-collapsing models, the electron fraction shows the highest peak value, at $Y_e \sim 0.33$.

3.2 Nucleosynthesis yields

We use the output of the nucleosynthesis calculations described in Sec. 2.3 to characterize the composition in the ejecta. We focus on the final abundances, which are representative of the ejecta composition as it eventually contributes to the galaxy enrichment.

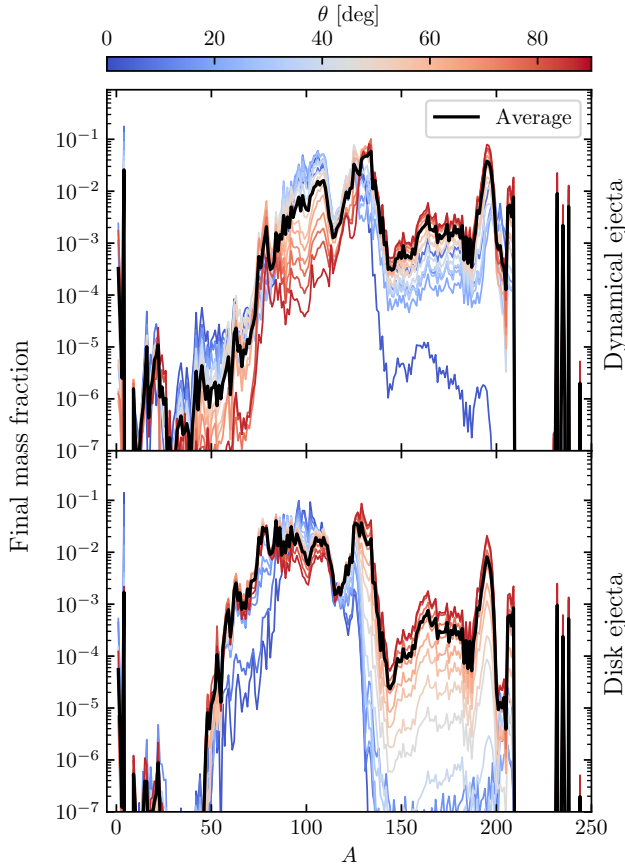


Figure 5. Final abundance patterns in the dynamical ejecta (top panel) and the early disk ejecta (bottom panel), relative to different polar angles θ for the model m_S^* . Each pattern is obtained through a mass-weighted average of the yields of all the tracers within the corresponding angular bin centered in θ . The overall mass-weighted average of each ejecta component is reported in black.

Fig. 5 shows the average abundance pattern as a function of the polar angle θ for one representative model, i.e. m_S^* . Both in the dynamical ejecta and in the early disk ejecta, the composition is strongly dependent on the angular direction, due to the latitudinal anisotropy in the initial electron fraction, entropy, and velocity of the ejecta. As seen in Sec. 3.1, the material ejected has a lower electron fraction close to the equatorial plane and a higher electron fraction in the polar region. The distribution is wider in the case of the dynamical ejecta, as it comprehends also the very low $Y_e \lesssim 0.1$ material. This feature is directly reflected in the angular patterns, whereas at high latitudes the composition is generally dominated by lighter elements, while at low latitudes a stronger r-process occurs, due to the larger availability of free neutrons. Regarding the dynamical component, its equatorial pattern features both second and third r-process peak elements to constitute more than $\sim 20\%$ of the local material, together with a suppression of the first r-process peak. In contrast, the polar pattern shows an inverted scenario, with the first peak and the lighter elements enhanced, the second peak partially decreased and the third peak almost absent. However, while along the latitudinal direction there is a large variability in the abundance of light elements, we find that a considerable amount of heavy elements is still produced down to angles $\theta \sim 20^\circ$, despite the local higher average electron fraction. This has to be ascribed to the longer expansion

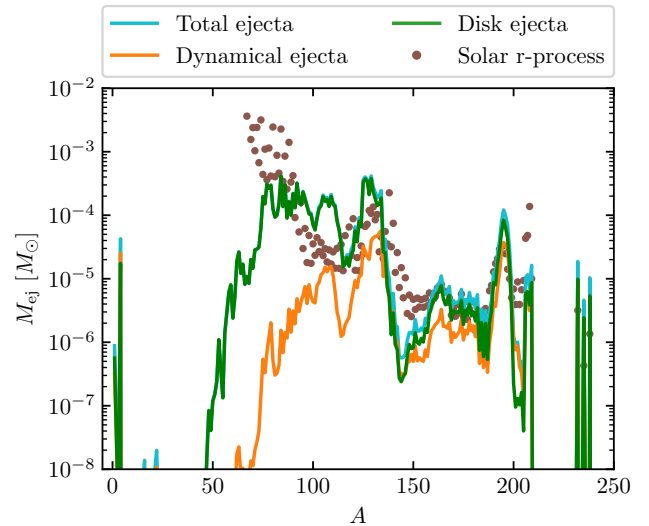


Figure 6. Final elemental mass distribution for the model m_S^* , along with the separate contributions from the dynamical ejecta and the disk ejecta. The solar r-process abundances (Lodders et al. 2009) normalized to the model abundance of Os ($A = 190$) are shown as reference.

timescale of the shock-heated component ($\tau \gtrsim 10$ ms), which allows for higher entropy r-process (see, e.g., Lippuner & Roberts 2015). On the other hand, in the early disk ejecta, the angular scatter in the first r-process peak is substantially reduced to one order of magnitude at most, while elements beyond the second peak show a more gradual variability, with the third peak still moderately present at the equator but progressively disappearing close to the pole. This behaviour is expected for mild ejecta velocities $\sim 0.1 c$, intermediate entropies $\sim 20 \text{ kJ baryon}^{-1}$, and for electron fractions lying close to the intermediate value $Y_e \sim 0.25$, denoting the strong sensitivity of the composition in this parameter region (similar results for the disk outflow composition were found in, e.g., Curtis et al. 2023). In this regard, we note that the presence of a moderate third peak for low latitudes in the disk ejecta is not particularly dependent on the separation criterion for the ejecta components that we adopted. For example, by increasing the extraction radius for the u_t evaluation to 400 km, the amount of low- Y_e material counting as dynamical ejecta instead of disk ejecta increases, due to the additional kinetic energy gained over its thermal energy, but it is found to be non-determinant in this context.

By the final simulated time, the overall composition is already mostly dominated by the disk ejecta, as evidenced in Fig. 6, which compares the total ejecta composition with the contributions from the dynamical ejecta and the early disk ejecta for the representative model m_S^* . The only exception is constituted by the model LS220[†], for which the final amounts of disk ejecta and dynamical ejecta are comparable. For all the models with a stable remnant, the dynamical component contribution to the final abundances is completely irrelevant for species with $50 \lesssim A \lesssim 130$. For $A \gtrsim 130$ we find only a minor impact, which is expected to be reduced further, as ejection from the disk continues in time. However the additional ejecta are also expected to have higher electron fractions, across the different phases in the disk evolution, thus roughly freezing the yields of elements heavier than $A \gtrsim 130$ (as found in, e.g., Martin et al. 2015; Magistrelli et al. 2024). Interestingly, Fig. 6 also shows that in all models the light species with $A \lesssim 50$, together with the heavier

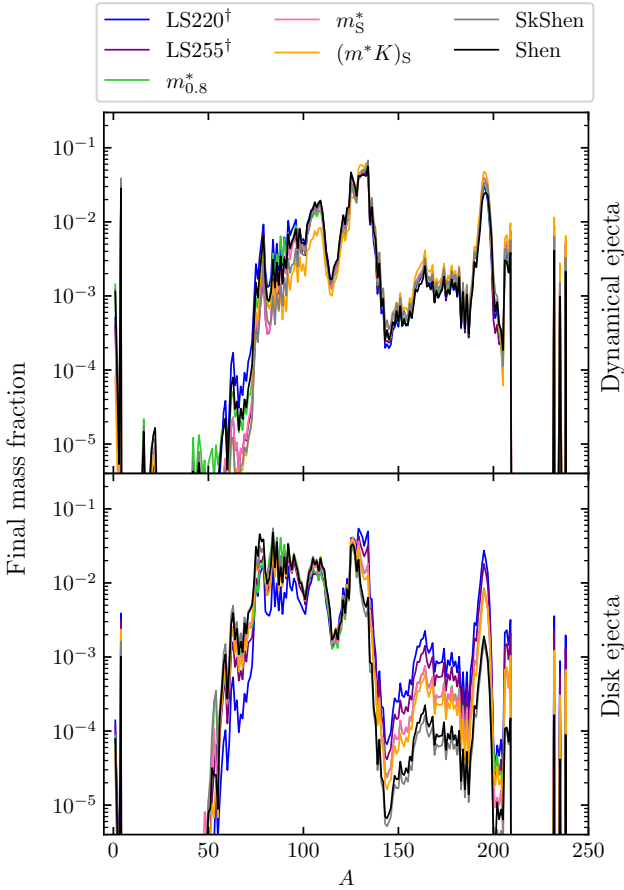


Figure 7. Final abundance pattern in the dynamical ejecta (top panel) and in the disk ejecta (bottom panel) for each EOS model. Each yield is obtained through a mass-weighted average of the yields of all the tracers belonging to the specific ejecta component from the corresponding model.

species with $200 \lesssim A \lesssim 205$, are still dominated by the contribution of the dynamical ejecta, as a result of the much greater specific yields of these elements returned in such component. This is due to the larger spread in the thermodynamic conditions of the dynamical material. For example, α particles are produced both in higher Y_e and s environments (polar shock-heated outflow), at the charged-particle reaction freeze-out, as well as in lower Y_e and s regions (tidal ejecta), also thanks to a contribution from the decay of heavy elements (see, e.g., [Perego et al. 2022b](#), for a recent work on this subject).

We also note that in the final patterns the ratio between second and third r-process peak elements is comparable to the one of the solar r-process ([Lodders et al. 2009](#)). Rare earth elements are decently reproduced, while the second peak only roughly agrees with the solar one, being narrower for all models. Elements with $130 \lesssim A \lesssim 155$ are systematically underproduced, which can most-likely be attributed to the current uncertainties in the nuclear inputs of the model ([Horowitz et al. 2019](#); [Cowan et al. 2021](#)). In addition, there is no agreement for elements with $A \lesssim 115$, however, in such region, viscous disk ejecta from the same neutron star merger event or ejecta from other astrophysical sources are likely to contribute as well.

In general, when comparing the final abundances across the different models, we find that the dynamical ejecta host a robust r-process pattern in all cases, varying at most of a factor of a few for elements

heavier than $A \sim 110$ (see Fig. 7). Greater variability is found for elements with $A \lesssim 110$, with up to one order of magnitude scatter for the first r-process peak. The production of rare earth and third peak elements is slightly enhanced moving from the Shen to the $(m^*K)_S$ model, for two reasons:

- the gradually increasing amount of tidal material expelled, characterized by very low electron fractions $Y_e \leq 0.1$ at equatorial angles of ejection (see top panels in Fig. 4), systematically creates such species;
- these species are also produced in the increasing shock-heated component, by matter with $0.1 \leq Y_e \leq 0.3$ and a sufficiently broad range of entropies and expansion timescales.

Fig. 8 shows the total ejected mass of a series of elements, divided into the contributions from the tidal, shock-heated and disk ejecta components. Within the dynamical ejecta, the contribution to the heavy elements production from the shock-heated component is dominant in most cases. Even for lanthanides such as Ce or Eu, the tidal contribution constitutes at most only half of the total yield. Therefore, for these elements a decrease in the amount of tidal ejecta is partially compensated by the increase in shock-heated ejecta. The first r-process peak region and lighter elements instead exhibit a trivial enhancement for greater amounts of shock-heated ejecta, as in the LS220[†], LS255[†] and $m_{0.8}^*$ models. However, the precise yields are substantially sensitive to the specific conditions found in this ejecta component. In particular, across different models we find variations in the ratio of elements already within the same group, such as between Fe and Ni or Sr and Zr. Therefore, for the dynamical ejecta, the amount of heavy elements produced in a strong r-process as well as the amount of lighter elements, hardly show any evident correlation with the deeper model parameters that characterize the original nuclear matter. This statement could be revised in absence of the heterogeneous shock-heated ejecta, as it would happen in a black hole - neutron star (BHNS) merger or a prompt BH formation case, in which only the tidal ejecta could dynamically emerge.

Regarding the disk ejecta yields, the $m_{0.8}^*$, SkShen and Shen models typically return the highest amount of light elements up to the first r-process peak, while second and third peak are produced more in models such as LS220[†] and LS255[†] (see both Fig. 7 and Fig. 8). Notably, however, the average initial Y_e is not a precise proxy for the final abundances, as the latter depend on the details of the Y_e distribution. For example, while the relative amount of iron group elements roughly follows the average Y_e , first peak elements are remarkably more sensitive to the position of the maximum in the Y_e distribution. Furthermore, as visible in Fig. 9, the model $m_{0.8}^*$ has among the highest values of average Y_e and position of the maximum in the Y_e distribution, but it still produces lanthanides yields which are comparable to the model $(m^*K)_S$.

In turn, the Y_e distribution evolves with the total amount of ejecta, since the initial conditions in the expelled material vary with time. Thus, the production of heavy elements across different models is less robust in the disk ejecta compared to the dynamical ejecta. On one side, this can be connected to the relative subdominance of a very low Y_e contribution within this channel, and on the other side to the lower velocity and entropy conditions, which can help building up most of the species already at high temperatures, depending on the specific Y_e . In general, the relative abundance of heavy elements only roughly scales inversely with the amount of disk ejecta, which are constituted by mixed- Y_e material. It could be reasonable to extend this scaling relation to the general stiffness of the EOS, but more data is necessary in order to verify this possibility.

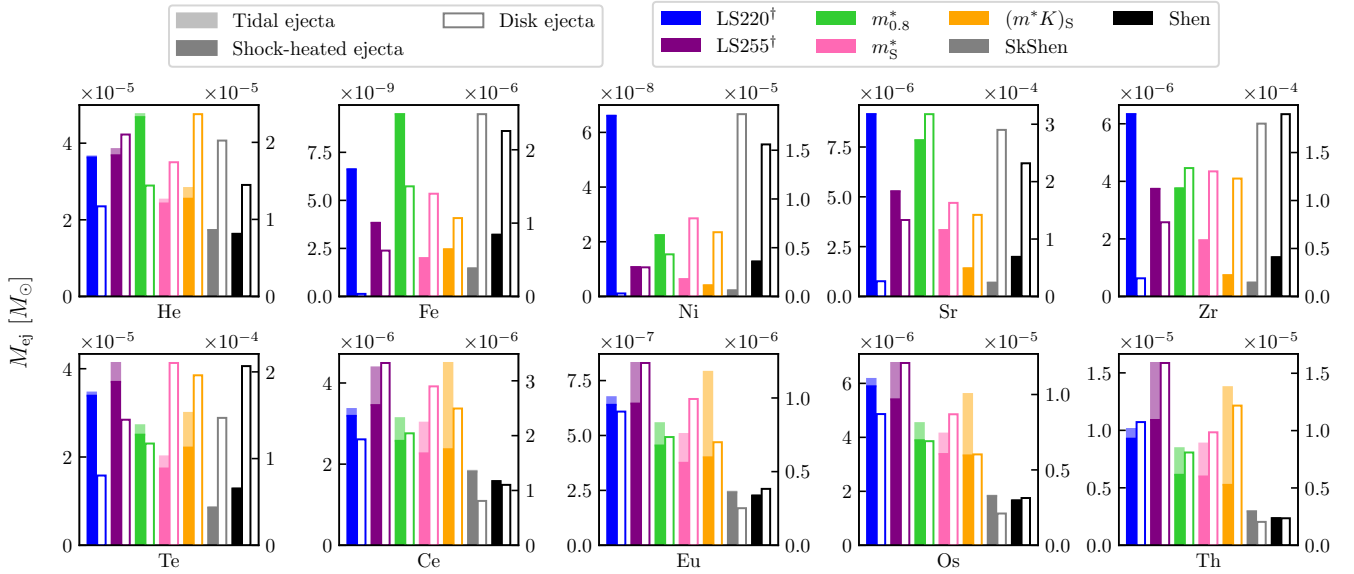


Figure 8. Final mass of a set of elements in the dynamical ejecta (left axis) and the disk ejecta (right axis) for each EOS model. For the dynamical ejecta, the contributions from the tidal and the shock-heated component are shown.

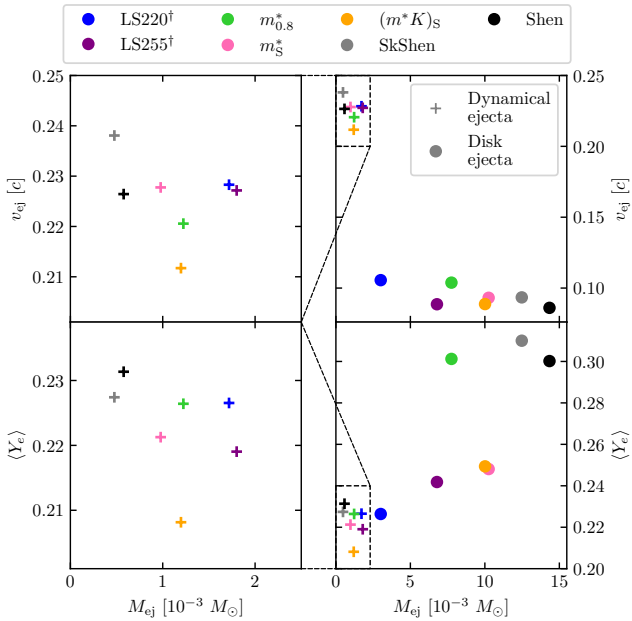


Figure 9. Dynamical ejecta and disk ejecta for each EOS model, represented in the space of total mass vs average velocity (top panel) and vs average electron fraction (bottom panel)

3.3 Kilonova light curves

Given the ejecta properties obtained from the extracted sets of tracers (Sec. 3.1) and the corresponding nucleosynthesis (Sec. 3.2), we now investigate the subsequent thermal KN emission. We compute the bolometric and color light curves within ~ 10 days post-merger using our anisotropic framework (Sec. 2.4), and we investigate the potential impact of the EOS on this transient. The ejecta scheme depicted in Fig. 10 is useful to understand which ejecta features are

carried over to the KN model. By construction, the latter simplifies the ejecta structure in order to solve analytically the radiative transfer problem. All models display an approximately prolate ejecta shape, with material in the polar region being typically 10% c faster than the equatorial direction. However, the density significantly decreases at higher latitudes, and, as a result, fewer and lower mass tracers populate the polar angular bins. Excluding outliers, this population shows a much narrower velocity distribution. Concurrently, the computed average opacities reflect the compositional variety of each component:

- a wider opacity range, varying from $\sim 2 \text{ cm}^2 \text{ g}^{-1}$ at the pole to $\sim 30 \text{ cm}^2 \text{ g}^{-1}$ at the equator, is found in the external, dynamically driven ejecta layers;
- a shorter opacity range, with values between $\sim 2 \text{ cm}^2 \text{ g}^{-1}$ and $\sim 10 \text{ cm}^2 \text{ g}^{-1}$, is observed in the internal regions originating from the disk.

As a consequence, the radial opacity profile decreases with larger radii at high latitudes, and it instead increases significantly with the radius at lower latitudes, potentially inducing the lanthanides curtain effect (see, e.g., Kasen et al. 2015; Wollaeger et al. 2018). According to the latter, bluer radiation can be shielded from an hypothetical edge-on observer ($\theta_{\text{view}} = 90^\circ$) by the lanthanide-rich material in the outermost layers of the ejecta.

With these features being roughly common to all the considered models, several aspects of the resulting emission are found persistent, regardless of the EOS employed. First of all, the bolometric luminosity peaks between 1 and 3 days, when the ejecta has expanded enough for its average optical depth to become comparable to the mean photon diffusion path. At that time the ejecta radiates with a rate of a few $10^{40} \text{ erg s}^{-1}$, catching up with the instantaneous energy deposition from the radioactive heating from r-process material. However, we note that the specific values of peak magnitude and timescale are sensitive to the total amount and type of ejecta produced in the merger event. As investigated further in Sec. 3.4, we expect the luminosity peak to shift to later times and to be brighter, once the disk ejecta

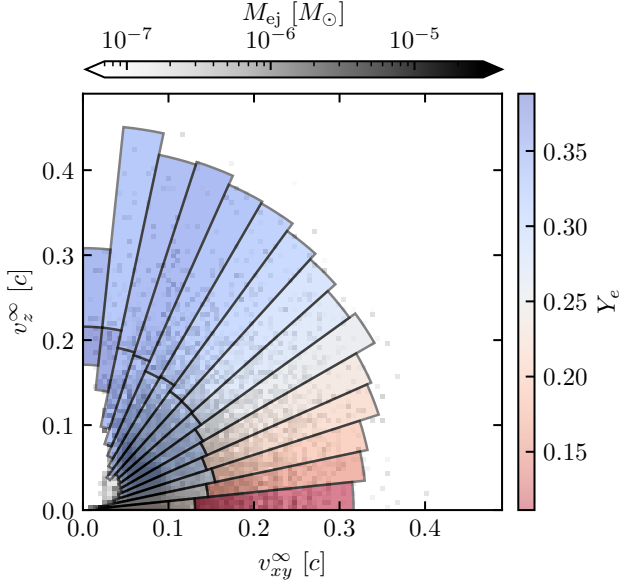


Figure 10. Scheme of the ejecta from the model m_S^* , as it is read by the semi-analytic KN model. Each sector represents a different angular bin, where the model is run on a ray-by-ray basis, with its boundaries in the radial direction being defined by the mass-weighted 1% and 99% percentiles of the tracers distribution. Each sector is divided into two zones, characterized by a different average gray opacity, which is parametrized with the local value of electron fraction, following Tanaka et al. (2020). The division between the two bin zones is obtained by averaging the position of the interface between the dynamical ejecta and the disk ejecta components. The ejecta mass histogram is shown as reference in gray in the background.

contribution is fully accounted for, because of the additional fuel provided to power the KN emission. As visible in Fig. 11, within the peak timescale, the total luminosity of the transient is dominated by the contribution of the ejecta regions at intermediate latitudes. In these regions, the balance between the local higher density and the lower material opacity is optimal. In fact, on one hand the fraction of energy emerging from the strictly polar region at its peak is at least one order of magnitude lower than from the equator, due to the very low amount of mass ejected in such direction. On the other hand, the equatorial contribution is characterized by a higher opacity as a result of the higher concentration of lanthanides, causing the radiation to be trapped for longer times and to be released at lower temperatures. Red photons eventually escape after a few days, when the overall emission has passed its peak, and become the dominant contribution. Notably, the considerable diffusion of a large variety of heavy elements throughout the ejecta and the subsequent dominance of their β -decay has the effect of suppressing any peculiar feature in the average radioactive heating rates, within the time frame of the KN photospheric phase. Such features would include the decay of particularly abundant lighter nuclear species, potentially visible in a weak r-process scenario, or the signature of fissioning nuclei, which do not emerge within the first ~ 15 days post-merger.

As described in Sec. 2.4, in order to compute the color evolution, we approximate the emission continuum with a standard black-body spectrum emerging from the ejecta photosphere and parametrized by an effective photospheric temperature T_{ph} . This approximation was found to be reasonable within a few days post-merger in the case of AT2017gfo, since in this time frame the presence of specific spectral

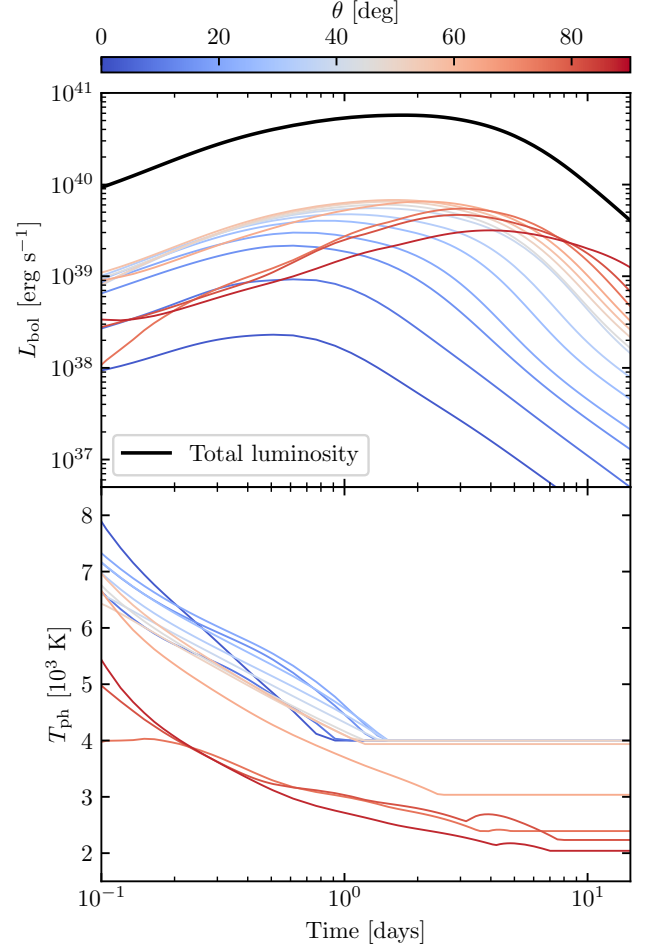


Figure 11. Total bolometric luminosity for the model m_S^* , along with the contribution coming from different angular bins (top panel). Effective photospheric temperature evolution as a function of the ejecta angle for the same model (bottom panel). A composition-dependent floor value is applied to the temperature in order to account for recombination in the late expanding ejecta.

features has a negligible impact on the overall evolution of the color curves (Smartt et al. 2017; Watson et al. 2019). At higher latitudes, where the local photosphere recedes inwards faster, the photospheric temperatures are instantaneously higher than in proximity of the equator, and the resulting emission is bluer. In the considered time interval for the KN, average temperatures in the ejecta are found to be lower than ~ 10000 K. This allows us to employ the grey opacities suggested by Tanaka et al. (2020) and computed for low-level (I-IV) ionized atoms, as can be typically found at those temperatures and densities. On the contrary, a careful exploration of the early time emission would require more extensive opacity calculations, including higher ionization stages in significantly hotter material, as investigated by Banerjee et al. (2020, 2022, 2023).

The color evolution of the thermal transient for the representative m_S^* model is shown in Fig. 12. The impact of the ejecta mass and opacity structure is directly reflected in the relatively early dominance of the redder bands, which rapidly take over the bluer ones already within ~ 1 day post-merger. The emission in these bands is further boosted at later times by progressively looking at the ejecta from a more edge-on configuration, due to the maximization of the pro-

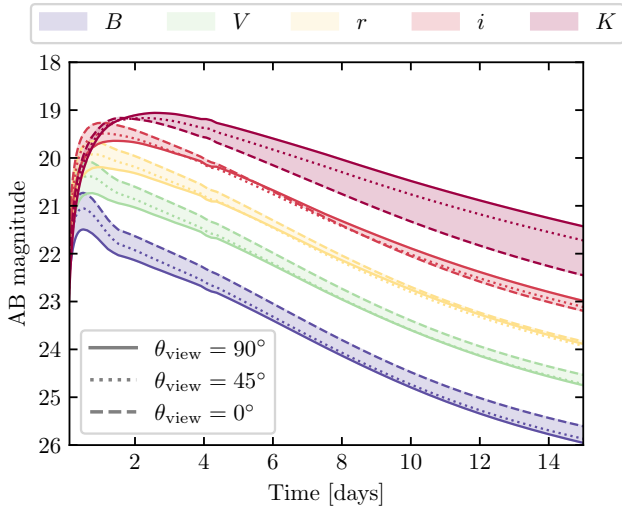


Figure 12. Broad-band light curves in various optical/IR filters for the model m_S^* . The dependency on the observer direction is shown, with distinct line styles indicating different viewing angles, varying from the polar direction (dashed lines) to the equatorial one (solid lines).

jected area corresponding to the more opaque ejecta region. On the contrary, bluer bands are generally multiple orders of magnitude less luminous, with a relatively weaker enhancement for a face-on view ($\theta_{\text{view}} = 0^\circ$). The main contribution to the latter emerges from a less dense environment with, however, an average opacity which never decreases down to typical values of Fe-like elements $\sim 0.1 \text{ cm}^2 \text{ g}^{-1}$. Nevertheless, once again, we recall that the role of the blue emission must be validated against the presence of additional moderate to high Y_e material, potentially ejected on longer timescales from the disk (see Sec. 3.4).

In terms of light curves, the most impacting effect of varying the EOS model is the overall amount of material expelled. As shown in Fig. 13, the emission brightness roughly follows the total ejecta mass, with a progressively brighter transient moving from the LS220[†] to the Shen model. The latter gains on LS220[†] more than one magnitude at peak time in all bands, while delaying the peak timescale of ~ 2 days. For all the EOS models, we observe a progressive broadening in the IR band variability associated with the observer viewing angle. This feature derives from the faster fading of the polar contribution with respect to the equatorial one. Concurrently, the trend is inverted for the bluer bands, with a gradual isotropization of the emission, due to the disappearance of the initially enhanced blue polar contribution. The effect is slower for the LS220[†] model, as a result of the greater general anisotropy produced by its dynamical ejecta coupled with the smaller disk ejecta. Among the different models, $m_{0.8}^*$ is the one generating the bluer and faster evolving transient, due to the small relative amount of lanthanides. The Shen and SkShen have similar compositions, but they shine longer thanks to the additional disk ejecta mass. On the other hand, with respect to similar models, $(m^*K)_S$ misses part of the early blue emission because the lanthanides curtain extends to relevantly higher latitudes.

In the context of an observed emission, the primary correlation between its brightness and the ejecta mass can be used as a constraint on the general EOS stiffness, as already pointed out by, e.g., Bauswein et al. (2013); Radice et al. (2018c). Such a dependence becomes particularly determinant when the collapse of the central remnant is involved, as in the case of the LS220[†] model. In principle,

combinations of nuclear matter properties concurring to the increase in the EOS softness could be disfavoured by the potential detection of a too bright KN, although a similar effect could also be achieved by an asymmetric enough initial binary. However, even in such case, it would not be clear how to constrain these nuclear matter properties individually, breaking the degeneracy that appears in the process.

3.4 Kilonova model extension

The final elemental yields in Sec. 3.2 and the KN light curves in Sec. 3.3 are sensitive to the ending time of our simulations. In order to determine whether this dependency impacts our results regarding the EOS effects, we model a hypothetical secular ejecta, stemming from the disk on longer timescales. We assume that roughly an additional 20% of the disk mass is ejected through secular mechanisms, as generally found in simulations of remnant disks accreting onto the central object (see, e.g., Hotokezaka et al. 2013; Just et al. 2015; Fernández et al. 2019; Fujibayashi et al. 2020; Just et al. 2021; Fahlman & Fernández 2022). Our assumption is supported by the fact that in all models the disk mass is found to be saturated by the end of the simulation. This results in a secular ejecta mass between $\sim 0.1 M_\odot$ and $\sim 0.06 M_\odot$, depending on the model. For such ejecta component, we adopt the properties of the last $\sim 10\%$ of disk mass ejected, i.e. we extract the velocity, entropy, electron fraction, and angular distributions of matter expelled approximately after ~ 40 ms post-merger. We thus obtain a secular ejecta where velocities and entropies closely follow the ones of the earlier disk ejecta, with an average velocity of $\sim 0.07 c$ and average entropy of $\sim 18 k_B \text{ baryon}^{-1}$. However, the ejection is mostly concentrated at angles $\geq 50^\circ$, and the electron fraction is distributed only between $0.25 \leq Y_e \leq 0.35$, with its peak shifted systematically to $Y_e \geq 0.3$. Therefore, the resulting composition does not include elements past the second r-process peak.

We show in Fig. 14 the KN light curves for the representative m_S^* model, obtained by taking the secular ejecta into account, in comparison to our previous results using the original ejecta. The additional late outflow enriches the slow, optically thick bulk of the ejecta with radioactive material exhibiting mild opacity values $\sim 5 \text{ cm}^2 \text{ g}^{-1}$. As a result, most of the injected energy is radiated away only at later times and lower frequencies, once the ejecta has expanded and cooled enough. The emission peak in the IR is thus shifted to ~ 4 days post-merger, with an increase in the peak luminosity of ~ 1 magnitude. The impact of the secular ejecta is less evident for times ≤ 1 day, when the emission is mostly dominated by the outer layers. In fact, the bluer emission component is affected only in its decaying phase, well after its peak. If we assume that this toy model broadly reproduces a plausible secular ejection in its main features, then this result confirms that in our models the early, blue phase of the KN is mainly dependent on the properties of the dynamical ejecta and of the early disk ejecta. However, we find less straightforward to identify a time frame where the light curves are completely determined by the sole dynamical ejecta component. Fig. 14 also shows the light curves obtained by ignoring all the ejecta components expelled after the dynamical ejecta. In such a case, the emission is affected already during the first hours after merger, with the largest variations for the bluer bands. The latter are found to be dimmer by around ~ 1 magnitude at 7 hours post-merger, with a faster fading, due to the lack of the contribution from lower opacity disk ejecta material. In light of this result, as pointed out in Sec. 3.3, early KN observations could help in constraining the general stiffness of the EOS, which is likely correlated to the amount of matter ejected in the first tens of milliseconds post-merger. Nevertheless, according to our findings, it would be difficult to extract information useful to constrain specific

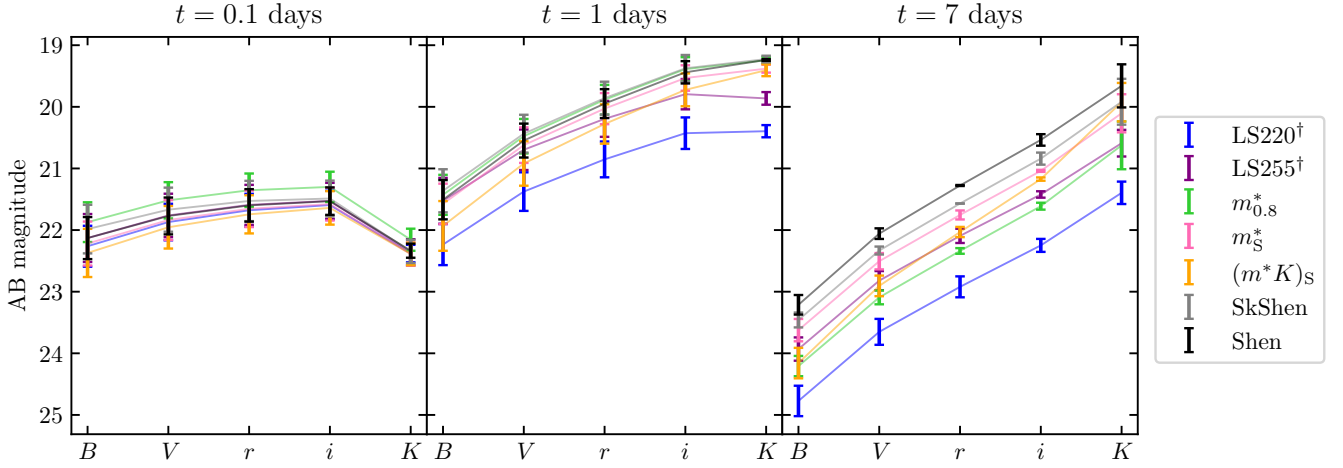


Figure 13. Color magnitudes at 0.1, 1 and 7 days in different filters for all the EOS models. The vertical bars indicate the variability related to the observer direction.

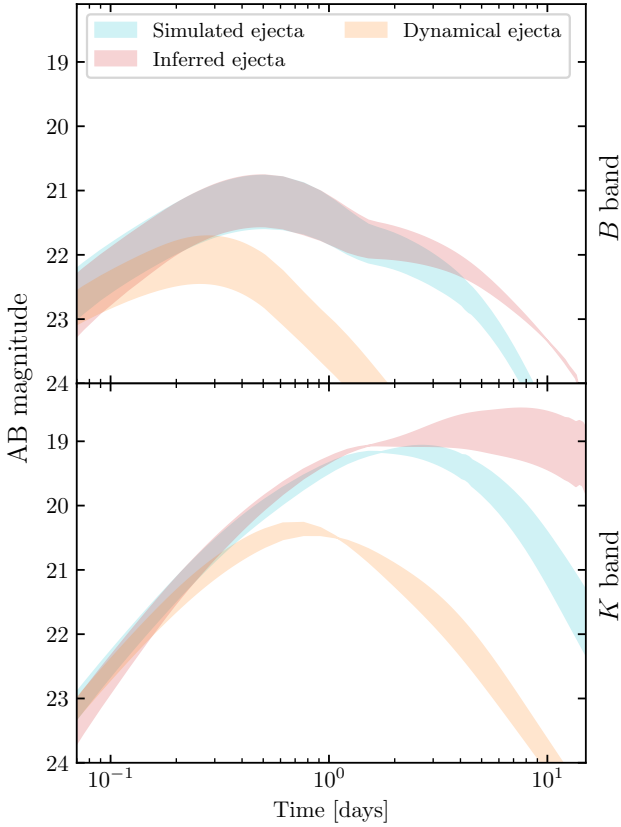


Figure 14. Broad-band light curves in the B and K filters for the model m_{S}^* , obtained by considering the ejecta from the simulation, in comparison to the result of including an additional secular ejecta component. The latter is modeled starting from the last portion of disk ejecta simulated and assuming an ejected mass of 20% of the disk mass. For visual reference, the light curves resulting from ignoring all the ejecta components past the dynamical ejecta are also shown. The spread of the curves indicates to the variability related to the observer direction.

nuclear matter properties, such as the incompressibility or the effective nucleon mass. Such an inference would be possible only in the hypothesis that there is a time frame in which the KN is uniquely determined by the dynamical ejecta contribution. This scenario would naturally exclude the formation of a massive accretion disk, and would favor a fast collapse of the remnant in order to suppress any neutrino-driven wind (see, e.g. [Perego et al. 2014a](#); [Radice et al. 2018d](#); [Kiuchi et al. 2019](#)). In any case, assuming an available early enough detection, the benchmark modeling would still require more detailed physics treatment, in primis on the opacity side.

4 CONCLUSION

In this work, we reprised the discussion on the EOS of nuclear matter, in relation to BNS merger events. We considered a set of BNS merger GRHD simulations employing different EOS models ([Yasin et al. 2020](#); [Jacobi et al. 2023](#)), and we investigated the associated nucleosynthesis and KN. For this purpose, we used the widely adopted tracer extraction method, in order to inform a nuclear reaction network, coupled with a ray-by-ray semi-analytic KN model.

We focused on the variation of the incompressibility parameter and of the effective nucleon mass, which affect the pressure and thermal evolution inside the merger remnant, leading to different amount of material ejected. For example, the softest models, LS175[†] and LS220[†], provoke a prompt and delayed collapse of the remnant respectively, and no or little ejecta is produced. On the other hand, for higher incompressibilities and lower effective masses, the overall ejection in the first tens of milliseconds post-merger is generally boosted, due to the longer-surviving oscillations of the remnant. Since these ejecta stem from the remnant disk with a broad range of initial electron fractions centered around $Y_e \sim 0.25$, the resulting nucleosynthesis drives an r-process with variable strength. Third peak elements are consistently found in the regions around the binary orbital plane, and the contribution from the disk outflows is comparable to the one of the dynamical ejecta. Variations in the final abundances across different EOS models are contained within one order of magnitude. Within the parameter range considered, these abundances exhibit a sensitivity in primis on the details of the initial Y_e distribution, which is not accurately captured by only one repre-

sentative value, such as the average Y_e . A stronger r-process pattern is found for smaller mass ejections, which roughly result from models with a softer EOS. However, a link to the nuclear matter parameters emerges only when considering the dynamical ejecta alone. In such context, the incompressibility and the effective nucleon mass show a connection with the amount of tidal and shock-heated ejecta respectively. In particular, the shock-heated component can significantly contribute to the production of elements as heavy as Eu or Pt. Therefore, a scenario where this channel is suppressed by a prompt BH presence could isolate the role of the incompressibility in producing such elements through purely tidal ejections.

Extending the discussion to the KN emission, light curves in the first dozen days post-merger are found relatively featureless, because of the widespread lanthanides-rich composition blending the radioactive energy deposition. The EOS directly impacts the emission peak magnitude, whereas stiffer EOSs generally produce more ejecta and brighter transients. Concurrently, the composition distribution affects the transient evolution, with the fastest evolving emission produced by the $m_{0.8}^*$ model, where a smaller amount of material ejected combines with a lower lanthanides pollution. KN light curves are the result of a complex chain of processes, and a large degeneracy emerges already when determining the sourcing ejecta properties. In light of the emission response to the EOS variation, tracing it back to the nuclear matter properties appears even more uncertain, and constrains can be reasonably put only on the overall EOS stiffness. Furthermore, light curves and final abundance patterns, as computed from the simulation output, are affected by an additional uncertainty, caused by the short simulated physical time frame. We expect potentially important differences, once the full ejection history is taken into account. Outflows from the disk after the simulated few tens of ms are expected to enrich the ejecta with higher Y_e material, and the light curves are altered in a way to substantially delay the emission peak. However, it appears clear that the disk ejecta play at least a partial role in producing the early blue KN component as well as the later red one. Therefore, we find difficult to isolate features in the KN emission which can be traced back to the sole dynamical ejecta, and, by extension, to details of the original nuclear EOS.

We interpret this result as a warning towards the study of the nuclear EOS using merger yields and KN light curves. This approach could still hold valuable information when combined to GW analysis, in extended, systematic studies, in order to face the large degeneracy of the problem.

ACKNOWLEDGEMENTS

The authors are grateful to A. Schwenk, F. M. Guercilena, K. Hotokezaka, M. Reichert, and S. Huth, for the valuable contributions and feedbacks in relation to the production of this work. This work is supported by the Deutsche Forschungsgemeinschaft (DFG, German Research Foundation, Project ID 279384907, SFB 1245), and by the State of Hesse within the Research Cluster ELEMENTS (Project ID 500/10.006).

DATA AVAILABILITY

The data concerning this work will be shared on reasonable request to the authors.

REFERENCES

- Abbott B. P., et al., 2017a, *Phys. Rev. Lett.*, 119, 161101
 Abbott B. P., et al., 2017b, *Astrophys. J.*, 848, L12
 Abbott B. P., et al., 2018, *Phys. Rev. Lett.*, 121, 161101
 Abbott B. P., et al., 2019, *Phys. Rev.*, X9, 011001
 Annala E., Gorda T., Kurkela A., Vuorinen A., 2018, *Phys. Rev. Lett.*, 120, 172703
 Arnett W. D., 1982, *Astrophys. J.*, 253, 785
 Banerjee S., Tanaka M., Kawaguchi K., Kato D., Gaigalas G., 2020, *Astrophys. J.*, 901, 29
 Banerjee S., Tanaka M., Kato D., Gaigalas G., Kawaguchi K., Domoto N., 2022, *Astrophys. J.*, 934, 117
 Banerjee S., Tanaka M., Kato D., Gaigalas G., 2023, preprint (ArXiv:2304.05810)
 Barbieri C., Salafia O. S., Perego A., Colpi M., Ghirlanda G., 2019, *Astron. Astrophys.*, 625, A152
 Barbieri C., Salafia O. S., Perego A., Colpi M., Ghirlanda G., 2020, *Eur. Phys. J.*, A56, 8
 Barnes J., Kasen D., 2013, *Astrophys. J.*, 775, 18
 Barnes J., Kasen D., Wu M.-R., Martinez-Pinedo G., 2016, *Astrophys. J.*, 829, 110
 Bauswein A., Janka H.-T., Oechslin R., 2010, *Phys. Rev.*, D82, 084043
 Bauswein A., Janka H., Hebel K., Schwenk A., 2012, *Phys. Rev.*, D86, 063001
 Bauswein A., Goriely S., Janka H.-T., 2013, *Astrophys. J.*, 773, 78
 Bauswein A., Just O., Janka H.-T., Stergioulas N., 2017, *Astrophys. J.*, 850, L34
 Bernuzzi S., Dietrich T., Nagar A., 2015, *Phys. Rev. Lett.*, 115, 091101
 Blacker S., Kochankowski H., Bauswein A., Ramos A., Tolos L., 2024, *Phys. Rev. D*, 109, 043015
 Bliss J., Witt M., Arcones A., Montes F., Pereira J., 2018, *Astrophys. J.*, 855, 135
 Bombaci I., Logoteta D., 2018, *Astron. Astrophys.*, 609, A128
 Bovard L., Rezzolla L., 2017, *Class. Quant. Grav.*, 34
 Bovard L., Martin D., Guercilena F., Arcones A., Rezzolla L., Korobkin O., 2017, *Phys. Rev.*, D96, 124005
 Bulla M., 2019, *Mon. Not. Roy. Astron. Soc.*, 489, 5037
 Bulla M., 2023, *Mon. Not. Roy. Astron. Soc.*, 520, 2558
 Camilletti A., et al., 2022, *Mon. Not. Roy. Astron. Soc.*, 516, 4760
 Combi L., Siegel D. M., 2023, *Astrophys. J.*, 944, 28
 Coughlin M. W., et al., 2018, *Mon. Not. Roy. Astron. Soc.*, 480, 3871
 Cowan J. J., Sneden C., Lawler J. E., Aprahamian A., Wiescher M., Langanke K., Martínez-Pinedo G., Thielemann F.-K., 2021, *Rev. Mod. Phys.*, 93, 15002
 Curtis S., Miller J. M., Fröhlich C., Sprouse T., Lloyd-Ronning N., Mumpower M., 2023, *Astrophys. J. Lett.*, 945, L13
 Cyburt R. H., et al., 2010, *Astrophys. J. Suppl.*, 189, 240
 Côté B., et al., 2019, *Astrophys. J.*, 875, 106
 Dietrich T., Coughlin M. W., Pang P. T. H., Bulla M., Heinzl J., Issa L., Tews I., Antier S., 2020, *Science*, 370, 1450
 Drischler C., Hebel K., Schwenk A., 2016, *Phys. Rev. C*, 93, 54314
 Drischler C., Hebel K., Schwenk A., 2019, *Phys. Rev. Lett.*, 122, 042501
 Eichler D., Livio M., Piran T., Schramm D. N., 1989, *Nature*, 340, 126
 Fahlman S., Fernández R., 2022, *Mon. Not. Roy. Astron. Soc.*, 513, 2689
 Fernández R., Tchekhovskoy A., Quataert E., Foucart F., Kasen D., 2019, *Mon. Not. Roy. Astron. Soc.*, 482, 3373
 Fields J., Prakash A., Breschi M., Radice D., Bernuzzi S., da Silva Schneider A., 2023, *Astrophys. J. Lett.*, 952, L36
 Flanagan E. E., Hinderer T., 2008, *Phys. Rev.*, D77, 021502
 Foucart F., Mösta P., Ramirez T., Wright A. J., Darbha S., Kasen D., 2021, *Phys. Rev. D*, 104, 1
 Freiburghaus C., Rembes J. F., Rauscher T., Kolbe E., Thielemann F. K., Kratz K. L., Pfeiffer B., Cowan J. J., 1999, *Astrophys. J.*, 516, 381
 Fujibayashi S., Wanajo S., Kiuchi K., Kyutoku K., Sekiguchi Y., Shibata M., 2020, *Astrophys. J.*, 901, 122
 Fujibayashi S., Kiuchi K., Wanajo S., Kyutoku K., Sekiguchi Y., Shibata M., 2023, *Astrophys. J.*, 942, 39

- Grossman D., Korobkin O., Rosswog S., Piran T., 2014, *Mon. Not. Roy. Astron. Soc.*, 439, 757
- Haas R., et al., 2020, The Einstein Toolkit, [doi:10.5281/ZENODO.4298887](https://doi.org/10.5281/ZENODO.4298887)
- Hammond P., Hawke I., Andersson N., 2021, *Phys. Rev. D*, 104, 103006
- Hebelner K., Bogner S. K., Furnstahl R. J., Nogga A., Schwenk A., 2011, *Phys. Rev. C*, 83, 031301
- Hinderer T., Lackey B. D., Lang R. N., Read J. S., 2010, *Phys. Rev.*, D81, 123016
- Horowitz C. J., et al., 2019, *Journal of Physics G: Nuclear and Particle Physics*, 46, 083001
- Hotokezaka K., Nakar E., 2020, *Astrophys. J.*, 891, 152
- Hotokezaka K., Kiuchi K., Kyutoku K., Okawa H., Sekiguchi Y.-i., et al., 2013, *Phys. Rev.*, D87, 024001
- Hotokezaka K., Kyutoku K., Sekiguchi Y.-i., Shibata M., 2016, *Phys. Rev.*, D93, 064082
- Jacobi M., Guercilena F. M., Huth S., Ricigliano G., Arcones A., Schwenk A., 2023, *Mon. Not. Roy. Astron. Soc.*, 527, 8812
- Just O., Bauswein A., Pulpillo R. A., Goriely S., Janka H. T., 2015, *Mon. Not. Roy. Astron. Soc.*, 448, 541
- Just O., Goriely S., Janka H.-T., Nagataki S., Bauswein A., 2021, *Mon. Not. Roy. Astron. Soc.*, 509, 1377
- Kasen D., Barnes J., 2019, *Astrophys. J.*, 876, 128
- Kasen D., Fernández R., Metzger B., 2015, *Mon. Not. Roy. Astron. Soc.*, 450, 1777
- Kasen D., Metzger B., Barnes J., Quataert E., Ramirez-Ruiz E., 2017, *Nature*, 551, 80
- Kiuchi K., Kyutoku K., Shibata M., Taniguchi K., 2019, *Astrophys. J.*, 876, L31
- Lattimer J. M., Schramm D. N., 1974, *Astrophys. J. Lett.*, 192, L145
- Lattimer J. M., Swesty F. D., 1991, *Nucl. Phys.*, A535, 331
- Li L.-X., Paczynski B., 1998, *Astrophys. J.*, 507, L59
- Lippuner J., Roberts L. F., 2015, *Astrophys. J.*, 815, 82
- Lippuner J., Roberts L. F., 2017, *Astrophys. J. Suppl.*, 233, 18
- Lodders K., Palme H., Gail H.-P., 2009, in *Martinsen W., Trümper J., eds*, , Vol. 4B, *Solar System*. Springer Berlin Heidelberg, Berlin, Heidelberg, pp 712–770, [doi:10.1007/978-3-540-88055-4_34](https://doi.org/10.1007/978-3-540-88055-4_34)
- Ludlam R. M., et al., 2022, *Astrophys. J.*, 927, 112
- Magistrelli F., Bernuzzi S., Perego A., Radice D., 2024, preprint (ArXiv:2403.13883)
- Margalit B., Metzger B. D., 2017, *Astrophys. J.*, 850, L19
- Martin D., Perego A., Arcones A., Thielemann F.-K., Korobkin O., Rosswog S., 2015, *Astrophys. J.*, 813, 2
- Metzger B. D., 2020, *Living Rev. Rel.*, 23, 1
- Metzger B. D., Fernández R., 2014, *Mon. Not. Roy. Astron. Soc.*, 441, 3444
- Metzger B., Martinez-Pinedo G., Darbha S., Quataert E., Arcones A., et al., 2010, *Mon. Not. Roy. Astron. Soc.*, 406, 2650
- Miller M. C., et al., 2019, *Astrophys. J.*, 887, L24
- Miller M. C., et al., 2021, *Astrophys. J. Lett.*, 918, L28
- Möller P., Sierk A. J., Ichikawa T., Sagawa H., 2016, *Atom. Data Nucl. Data Tabl.*, 109-110, 1
- Morozova V., Piro A. L., Renzo M., Ott C. D., Clausen D., Couch S. M., Ellis J., Roberts L. F., 2015, *Astrophys. J.*, 814, 63
- Most E. R., Raithel C. A., 2021, *Phys. Rev. D*, 104, 124012
- Most E. R., Papenfort L. J., Dexheimer V., Hanauske M., Schramm S., Stöcker H., Rezzolla L., 2019, *Phys. Rev. Lett.*, 122, 061101
- Nedora V., Bernuzzi S., Radice D., Perego A., Endrizzi A., Ortiz N., 2019, *Astrophys. J.*, 886, L30
- Nedora V., Radice D., Bernuzzi S., Perego A., Daszuta B., Endrizzi A., Prakash A., Schianchi F., 2021a, *Mon. Not. Roy. Astron. Soc.*, 506, 5908
- Nedora V., et al., 2021b, *Astrophys. J.*, 906, 98
- Nedora V., et al., 2022, *Class. Quant. Grav.*, 39, 015008
- Neilsen D., Liebbling S. L., Anderson M., Lehner L., O'Connor E., et al., 2014, *Phys. Rev.*, D89, 104029
- Panov I., Freiburghaus C., Thielemann F.-K., 2001, *Nucl. Phys. A*, 688, 587
- Perego A., Rosswog S., Cabezón R. M., Korobkin O., Käppeli R., Arcones A., Liebendörfer M., 2014a, *Mon. Not. Roy. Astron. Soc.*, 443, 3134
- Perego A., Gafton E., Cabezón R., Rosswog S., Liebendörfer M., 2014b, *Astron. Astrophys.*, 568, A11
- Perego A., Radice D., Bernuzzi S., 2017, *Astrophys. J.*, 850, L37
- Perego A., Bernuzzi S., Radice D., 2019, *Eur. Phys. J.*, A55, 124
- Perego A., Logoteta D., Radice D., Bernuzzi S., Kashyap R., Das A., Padamata S., Prakash A., 2022a, *Phys. Rev. Lett.*, 129, 032701
- Perego A., et al., 2022b, *Astrophys. J.*, 925, 22
- Pinto P. A., Eastman R. G., 2000, *Astrophys. J.*, 530, 744
- Radice D., Rezzolla L., 2012, *Astron. Astrophys.*, 547, A26
- Radice D., Bernuzzi S., Del Pozzo W., Roberts L. F., Ott C. D., 2017, *Astrophys. J.*, 842, L10
- Radice D., Perego A., Bernuzzi S., Zhang B., 2018a, *Mon. Not. Roy. Astron. Soc.*, 481, 3670
- Radice D., Perego A., Zappa F., Bernuzzi S., 2018b, *Astrophys. J.*, 852, L29
- Radice D., Perego A., Hotokezaka K., Fromm S. A., Bernuzzi S., Roberts L. F., 2018c, *Astrophys. J.*, 869, 130
- Radice D., Perego A., Hotokezaka K., Fromm S. A., Bernuzzi S., Roberts L. F., 2018d, *Astrophys. J.*, 869, 130
- Raithel C. A., Ozel F., Psaltis D., 2019, *Astrophys. J.*, 875, 12
- Ravi V., Lasky P. D., 2014, *Mon. Not. Roy. Astron. Soc.*, 441, 2433
- Reichert M., et al., 2023, *Astrophys. J. Suppl.*, 268, 66
- Rezzolla L., Most E. R., Weih L. R., 2018, *Astrophys. J.*, 852, L25
- Ricigliano G., Perego A., Borhanian S., Loffredo E., Kawaguchi K., Bernuzzi S., Lippold L. C., 2024, *Mon. Not. Roy. Astron. Soc.*, 529, 647
- Riley T. E., et al., 2019, *Astrophys. J.*, 887, L21
- Riley T. E., et al., 2021, *Astrophys. J. Lett.*, 918, L27
- Rosswog S., Sollerman J., Feindt U., Goobar A., Korobkin O., Wollaeger R., Fremling C., Kasliwal M. M., 2018, *Astron. Astrophys.*, 615, A132
- Salmi T., et al., 2022, *Astrophys. J.*, 941, 150
- Schneider A. S., Roberts L. F., Ott C. D., 2017, *Phys. Rev.*, C96, 065802
- Sekiguchi Y., Kiuchi K., Kyutoku K., Shibata M., Taniguchi K., 2016, *Phys. Rev.*, D93, 124046
- Shen H., Toki H., Oyamatsu K., Sumiyoshi K., 1998, *Nucl. Phys.*, A637, 435
- Shibata M., Fujibayashi S., Hotokezaka K., Kiuchi K., Kyutoku K., Sekiguchi Y., Tanaka M., 2017, *Phys. Rev.*, D96, 123012
- Shingles L. J., et al., 2023, *Astrophys. J. Lett.*, 954, L41
- Sieverding A., Waldrop P. G., Harris J. A., Hix W. R., Lentz E. J., Bruenn S. W., Messer O. E. B., 2023, *Astrophys. J.*, 950, 34
- Smartt S. J., et al., 2017, *Nature*, 551, 75
- Steiner A. W., Hempel M., Fischer T., 2013, *Astrophys. J.*, 774, 17
- Tanaka M., Hotokezaka K., 2013, *Astrophys. J.*, 775, 113
- Tanaka M., Kato D., Gaigalas G., Kawaguchi K., 2020, *Mon. Not. Roy. Astron. Soc.*, 496, 1369
- Tews I., Margueron J., Reddy S., 2018, *Phys. Rev.*, C98, 045804
- Thielemann F. K., Eichler M., Panov I. V., Wehmeyer B., 2017, *Ann. Rev. Nucl. Part. Sci.*, 67, 253
- Watson D., et al., 2019, *Nature*, 574, 497
- Winteler C., Kaeppli R., Perego A., Arcones A., Vassetz N., Nishimura N., Liebendoerfer M., Thielemann F.-K., 2012, *Astrophys. J. Lett.*, 750, L22
- Wollaeger R. T., et al., 2018, *Mon. Not. Roy. Astron. Soc.*, 478, 3298
- Wu Z., Ricigliano G., Kashyap R., Perego A., Radice D., 2022, *Mon. Not. Roy. Astron. Soc.*, 512, 328
- Yasin H., Schäfer S., Arcones A., Schwenk A., 2020, *Phys. Rev. Lett.*, 124, 92701

APPENDIX A: TRACERS CLUSTERING AND SELECTION

In the context of explosive nucleosynthesis scenarios, the outflow hosting the nucleosynthesis process can be analysed through a number of tracers large enough in order to resolve all the relevant structural and compositional features. Despite the relatively low computational cost of a single nuclear reaction network calculation, the latter is often repeated thousands to even millions of times for a complete outflow characterization. However, among the many local thermodynamic initial conditions that are found within a single explosion event, some of them return similar if not nearly identical nucleosynthesis outcomes. It is therefore possible to significantly reduce the

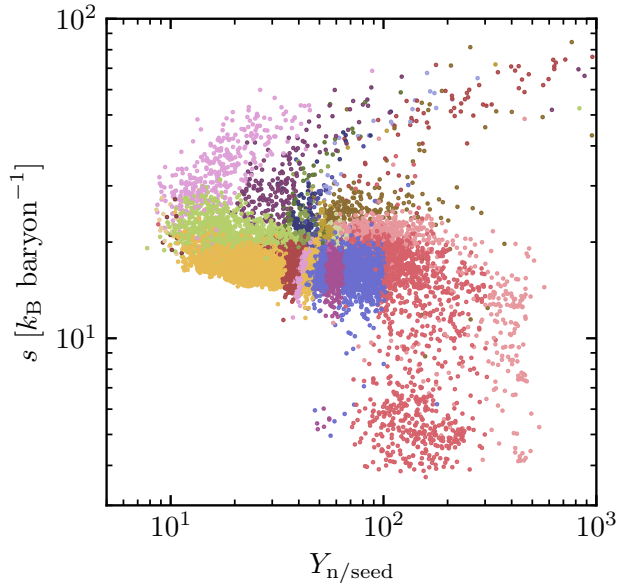


Figure A1. Example of tracers clustering based on final abundances. The tracers are obtained from the model m_S^* and are depicted as dots in the parameter space formed by the neutron-to-seed ratio and the specific entropy evaluated at ~ 5.8 GK. Each color represents a different cluster, characterized by similar abundance patterns with less than one order of magnitude difference at the abundance peaks.

amount of necessary information derived from hydrodynamical simulations, by identifying and grouping such conditions on the basis of the final yields (see, e.g., [Bliss et al. 2018](#), for a similar analysis).

In our approach, we first focus on a single simulation output (we choose the m_S^* model as representative) and we run the nuclear reaction network on the full collection of tracers. The resulting final abundances are then analysed by employing a bottom-up hierarchical clustering procedure, in which we define a distance d between two tracers x and y as:

$$d_{x,y} := \sum_{i:A_i > 50} |\log(X_i^x) - \log(X_i^y)|, \quad (\text{A1})$$

where X_i is the final mass fraction of the species i and the sum runs over the species of interest for the r-process, with mass number $A_i > 50$. By tuning a minimum average distance between two separate clusters, we gather in the same group the abundance patterns that show analogous features, with less than one order of magnitude difference at the abundance peaks, and we obtain a few tens (~ 35) of separate clusters.

Subsequently, we choose a parameter space where these clusters live in connected and distinguishable regions. In principle, the r-process nucleosynthesis is basically determined by the value of the neutron-to-seed ratio $Y_{n/seed} = \frac{Y_n}{Y_{seed}}$ at the onset of the process, around ~ 3 GK, with Y_n the abundance of free neutrons and Y_{seed} that of seed nuclei. While at this temperature $Y_{n/seed}$ can be exactly computed only using a reaction network, we approximately infer a representative $Y_{n/seed}$ by evaluating it in NSE at a higher temperature of ~ 5.8 GK, commonly associated to NSE freeze-out. Despite, within this temperature shift, charged particle reactions can substantially alter the exact $Y_{n/seed}$ value, we find that the error in this estimation does not qualitatively affect the clusters mapping. We also find that clusters are well-reproduced when represented in a parameter space

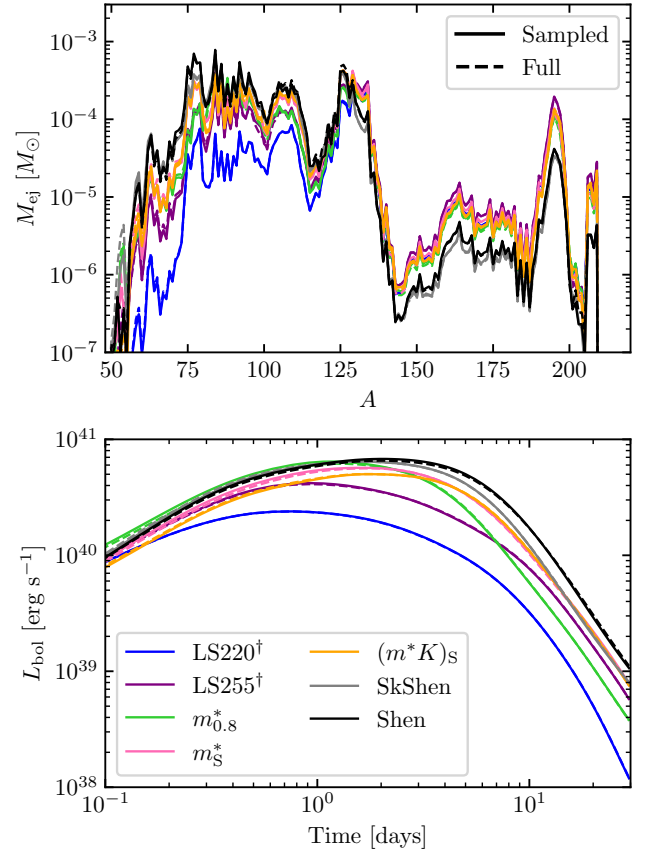


Figure A2. Final abundance pattern (top panel) and bolometric luminosity (bottom panel) for all the EOS models, as computed using the entire set of extracted tracers and the subset obtained following the sampling procedure, which is fitted to the model m_S^* .

formed by the specific entropy s at 5.8 GK, together with $Y_{n/seed}$, as shown in Fig. A1 for our trial model. In particular, tracers gather around a central region of interest with $Y_{n/seed} \sim 30 - 100$, where the highest variability of the nucleosynthesis outcomes is concentrated.

On the basis of this analysis, we construct a grid manually fitted to the cluster map, with a denser binning in the above inner region and a coarser binning in the outer regions, where abundances are less affected by the specific initial conditions. For each of our models, we employ this grid in order to map every simulation tracer to the correspondent cluster. We thus randomly select a variable number of representative tracers for each grid bin, and we use them to run our reduced nucleosynthesis calculations. The remaining tracers are then associated to the nucleosynthesis evolution of the closer representative tracer in the parameter space. We find that a 2D grid of 36 bins with 50 to 200 samples per bin is dense enough to reproduce the final results of each model with a good accuracy, as shown in Fig. A2. The obvious caveat to this approach is that, since its precision scales with the number of samples, local ejecta features can be under-resolved, especially in regions with an already low original number of tracers, e.g. in the low-density polar region. Nevertheless, our findings suggest that global features of the ejecta, such as the total yields or the KN emission, are the result of a broad average over all the different ejecta conditions, and as such they can be obtained already from a reduced amount of information.

This paper has been typeset from a $\text{\TeX}/\text{\LaTeX}$ file prepared by the author.